Available online at www.sciencedirect.com
SCIENCE DIRECT
Catalysis Today 109 (2005) 135–153
CATALYSIS TODAY
www.elsevier.com/locate/cattod

THERMIDOR: A new model for combined simulation of operations and optimization of catalysts in residues hydroprocessing units

Hervé Toulhoat [a,*], Damien Hudebine [c], Pascal Raybaud [b], Denis Guillaume [d], Stéphane Kressmann [c]

[a] *Direction Scientifique, IFP-Rueil, 1 & 4 Avenue de Bois-Préau, 92852 Rueil-Malmaison Cedex, France*
[b] *Direction Chimie et Physico-Chimie Appliquées, IFP-Rueil, 1 & 4 Avenue de Bois-Préau, 92852 Rueil-Malmaison Cedex, France*
[c] *Direction Procédés, IFP-Lyon, BP3, 69390 Vernaison, France*
[d] *Direction Catalyse et Séparations, IFP-Lyon, BP3, 69390 Vernaison, France*

Available online 30 September 2005

Abstract

Atmospheric or vacuum residues can be upgraded under high hydrogen pressure into valuable distillates and low sulfur fuel oils using several types of hydroprocessing units. Starting from such highly asphaltenic feeds, with the goal to achieve current very low sulfur targets (<0.3%) in fuels for export or subsequent upgrading by catalytic cracking technologies, fixed bed technologies like the HYVAHL process are still the most efficient. This paper discusses some recent developments of HYVAHL, aiming at improved desulfurization levels and operating times. These improvements were helped by the predictions of a newly developed mathematical model called THERmal Monitoring for Isoperformance Desulfurization of Oil Residues (THERMIDOR). This model simulates the HYVAHL process operation along time on stream, taking into account the complex associations of guard bed materials and catalysts including particle size, activity, pore size and shape grading effects. A crucial non trivial achievement in THERMIDOR is the realistic representation of the two main catalyst deactivation mechanisms in residues hydroprocessing: coke and metals deposition. The model shows clearly the synergy between dedicated HDM (''chesnut bur'' type, larger mesopores, and macropores) and HDS (higher surface area and activity) catalysts. A very well defined optimum partition of the two catalysts is predicted and found in excellent agreement with the typical optimum determined from pilot plant experiments, and further implemented in commercial plants. The simulation results are successfully compared with representative operational data from a typical HYVAHL plant and reveal new insights on the complex catalyst deactivation phenomena involved in residue hydroprocessing.

Keywords: Hydroconversion; Residue; Hydrodesulfurisation; Hydroprocessing; Hydrodemetallation; Heterogeneous catalysts; Modelling

1. Introduction

Many million tonnes of fuels are produced in refineries every year, and a strong demand for very low sulfur fuel oil (LSFO 1 wt% S) is sustained on the market. This is mainly due to the evolution of the regulations imposing lower SO_x emissions for power plants, refineries and ships. Atmospheric residue (AR) and vacuum residue (VR) are the most difficult feeds to convert catalytically because they contain concentrated impurities like sulfur, nitrogen, asphaltenes and metals (essentially nickel and vanadium). The market demand for residue upgrading is the reduction of the sulfur content and some conversion into lighter products. In addition, deep hydrogenation and hydrodenitrogenation are more and more requested to meet the product specifications, notably for FCC pretreatment, and reduction of NO_x in power plants. Moreover, regulations on emissions will be even more drastic in the near future. This combination of trends will call for ever more severe hydroprocessing of residues.

While several kinds of residue upgrading processes are now commercially proven, such as fixed bed, moving bed and ebullated bed processes, the choice among the available technologies depends on the quality of feed to be processed. The hydrodesulfurization of residues in a fixed bed is still the

* Corresponding author.
E-mail address: herve.toulhoat@ifp.fr (H. Toulhoat).

0920-5861/$ – see front matter © 2005 Elsevier B.V. All rights reserved.
doi:10.1016/j.cattod.2005.08.023

most used. It is a well established upgrading process which requires specific catalysts. IFP and TOTAL have developed a fixed bed residue upgrading process using several fixed bed reactors in series, the HYVAHL process [1]. The lastest improvements developed by IFP utilize:

- a ''by-pass'' guard reactor or a permutable reactors system (PRS) in front of the classical fixed bed (Fig. 1),
- catalyst packages optimized for various feedstocks and process objectives.

The main problem for these new developments is to determine the proportion of catalysts to be used versus the client objectives. Several kinds of catalysts are generally used, each of them playing a specific role to achieve the following main functions:

- Disaggregation of large asphaltene molecules to enable removal of nickel and vanadium (HDM) and reduction of asphaltenes content, achieved by specific catalysts loaded in the first reactors. These catalysts must protect as much as possible from deactivation by HDM products the refining catalysts placed downstream.
- Hydrogenation and hydrogenolysis reactions for sulfur and nitrogen removal (HDS, HDN), and Conradson Carbon reduction, achieved by refining catalysts located in the last reactors, and therefore protected as much as possible by the HDM catalysts placed upstream.

A high hydrogen pressure is required in order to limit polycondensation reactions leading to coke formation.

In residues Ni + V contents are of the order of 100 ppm or more in the form of organometallic complexes. The hydrodemetallation reactions result in the deposition of metal sulfides (VS_x, NiS and mixed sulfides) as products inside the catalysts pores. These solid deposits build up to significant amounts over a few months. Because the HDM reactions are relatively fast and involve organometallic reactants of large sizes, intragranular mass transfer is largely controlled by diffusion, so that very steep concentration gradients of both reactants and solid products deposited may develop inside the catalysts grains. Usual hydroprocessing catalysts have small to medium mesopores which favor such gradients and are therefore subject to the well known pore mouth plugging phenomenon: they store metal sulfides with a poor efficiency and loose all activity abruptly after having captured not much than a few grams of metal sulfides per 100 g of fresh catalyst, which are concentrated in the very outer skin of the grains. Specific HDM catalysts are designed so as to reduce the diffusional limitations as far as possible and to provide plenty of pore volume to store the metal sulfides poisons: storage capacities up to 100 g of metal sulfides per 100 g of fresh catalyst have been demonstrated. Beside metal sulfides, a large amount of solid coke is also deposited inside the catalyst pores when residues are hydroprocessed. Indeed, these feedstocks concentrate asphaltenes, resins, sediments and have already undergone exposure to high temperatures at low pressures at the crude oil distillation stages, so that dehydrogenation and polycondensation reactions of heavy molecules have already begun. Upstream incidents, for instance temperature runaways at the distillation tower, may severely accentuate the coke forming potential of residues.

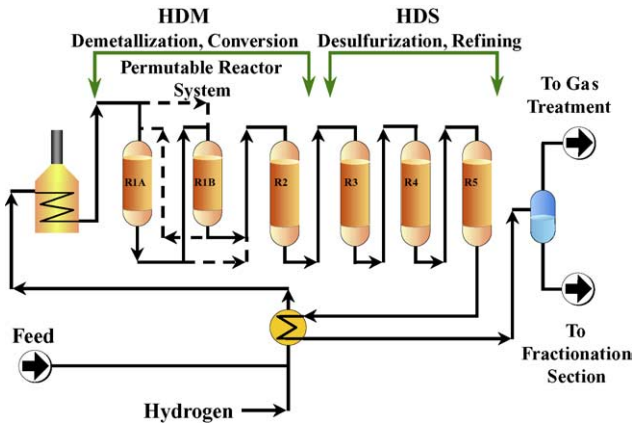

Fig. 1. HYVAHL process flow diagram.

In practice, in a HYVAHL multi-bed unit, the lead catalytic bed, loaded with special guard materials and a HDM catalyst, will be exposed to the highest concentration of metals and coke precursors, plus sediments and scales: it has therefore to function as both a filter and guard bed. It is observed that pressure drop increases much faster across this lead bed than across the following beds. One of the goals of the PRS system is to allow replacement of the fouled material in the lead bed as frequently as needed without interruption of operations. The PRS system offers moreover a good security against accidental degradations of the feedstock quality.

This very schematic overview of the HYVAHL process suffices to understand that it is crucial to find the optimal combination of catalysts, their optimal design and the optimal process control strategy in order to achieve the optimal return on investment in such huge hydroprocessing units (the typical order of magnitude is 1000 tonnes of catalyst for capacities of several tens of thousands of barrels per day). In periods of intense demand, as currently, this means basically the longest and smoothest possible uninterrupted operation periods. The catalysts activities in stabilised regime and resistance to deactivation by metals and coke are crucial in this respect. In view of the very complex nature of these phenomena, the optimization task is very delicate.

The purpose of the present paper is to demonstrate the interest of numerical simulations as an aid to this precise process design, and moreover as a guide for the improvement of existing catalysts or the research for new ones. THERmal Monitoring for Isoperformance Desulfurization Of Residua (THERMIDOR) was developed to achieve this goal.

We start in Section 2 with a rather detailed description of the underlying physical and physico-chemical principles in THERMIDOR, and their mathematical translation. The simulation algorithm and code architecture are then outlined.

We further demonstrate the ability of THERMIDOR in reproducing, for an accelerated ageing test at the bench scale, the evolutions of performances with time of two dedicated catalysts (A and B, for residue HDM and HDS, respectively). A

set of consistent basic input parameters for THERMIDOR is determined at this stage, which involves Boscan heavy crude as feedstock.

We then tackle the full scale problem, with the simulation of operations in a typical industrial HYVAHL unit: the simulation outputs are compared to real data, i.e. longitudinal weighted average bed temperature profiles as a function of time, and post-run analysis of used catalysts. A fair agreement is obtained with a minimal adjustment of simulation parameters to the particular properties of the VR feedstock involved in real operations. Most remarkably, we show that the optimal partition between the lead HDM catalyst, and the HDS catalyst, adopted at the industrial scale after extensive development work in the pilot plant, is neatly recovered by THERMIDOR simulations.

We end up with a discussion of the perspectives offered by the detailed simulations implemented in THERMIDOR, but also their limitations. Directions for improvements currently considered are also sketched in this conclusion.

2. Methods

2.1. Simulations

2.1.1. Introduction

All simulations were performed with the code THERMIDOR. This code simulates a catalytic hydrotreating unit as an association of plug flow trickle beds separated by quenching devices. The reactors can be considered isothermal or adiabatic, and simulations are run either at constant inlet temperature or at constant performance, monitoring inlet temperature in the latter case, in order to compensate for catalyst deactivation as time on stream elapses. This latter mode of monitoring corresponds to the industrial mode of operation of a large scale residues upgrading unit like those designed according to the HYVAHL process. The main novelty in THERMIDOR consists in the implementation of an elaborate description of the two main modes of heterogeneous catalysts deactivation under resid hydroprocessing conditions: coking, and metal sulfide deposition (mostly Ni and V sulfides). Both modes of deactivation affect, on the one hand the catalysts' intrinsic activities for the different reactions transforming the feedstock in hydrotreating conditions, and on the other hand the catalysts' textural properties (pore blockage). Since the kinetics of hydrotreating reactions involving high molecular weight reactants (''asphaltenes'' and ''resins'') are well known to be limited by intragranular mass transfer, concentration gradients will show up at the catalyst grain scale, as a result of the mixed regime. These gradients will change continuously with time on stream and axial position along the plug-flow unit, due to the local changes of textural properties (effective pore diameter, or equivalently void fraction and surface area) as coke and (Ni, V) sulfides build-up. In order to address this complexity, THERMIDOR includes two spatial scales in embedded loops: the grain scale, and the bed scale. The spherical or cylindrical symmetries are assumed at the grain scale, depending on the catalysts grain shapes (e.g. spherical pellets or cylindrical extrudates), leaving the fractional radius r as the local (grain scale) space variable, while the fractional axial position z suffices to describe the variation of properties between inlets and outlets of the plug-flow trickle beds.

2.1.2. General equations

The feedstock is represented by a set of $n \times p$ ''lumped'' reactive components where $1 \le i \le n$ is a chemical class, and $1 \le j \le p$ a reactivity class in the chemical class (e.g. j sulfur compounds lumps of different reactivity in the class ''sulfur compounds''). Reactions kinetics are implemented for each of the q catalysts loaded in series as a set of $n \times p \times q$ pseudo Langmuir–Hinshelwood type equations. These equations basically describe the hydrotreating reactions as first-order in the disappearing reactant, and inhibited by the adsorption of asphaltenes of type ''2'' (see Section 3.1.2 below for a justification of this choice). With $1 \le k \le q$ the rank of a catalyst, we have the following relation:

$$\rho_{ijk}(r,z,t) = k_{ijk}(r,z,t)S_k(r,z,t)\exp\left(\frac{E^{\pm}_{ijk}}{RT}\right) \times \frac{C^{\mathrm{l}}_{ij}(r,z,t)}{[1 + K^{\mathrm{ads}}_{\mathrm{A}2k}(T[z,t])C^{\mathrm{l}}_{\mathrm{A}2}(r,z,t)]} \quad (1)$$

In Eq. (1), the rate ρ_{ijk} is expressed as mole of reactant per unit volume of catalyst and unit time. $S_k(r,z,t)$ the local specific area of catalyst k at time t, so that the variables r and z have bounds relative to that catalyst ($r \le R^{\mathrm{G}}_k$ R^{G}_kbeing the grain radius for catalyst k, and $z^{\mathrm{in}}_k \le z \le z^{\mathrm{out}}_k$, z^{in}_k and z^{out}_k being, respectively, the positions of inlet and outlet of catalyst bed k along the z axis). The evolution of the local specific area is described by the deactivation model presented below. k_{ijk} is a local intrinsic rate constant at time t which depends on the nature of the catalytic surface. The latter is considered as a composite of the fresh surface, and deposited coke and (Ni, V) sulfides, with relative weights proportional to the local probabilities of an element of surface belonging to one of the three coexisting solid phases (the calculation of these probabilities will be discussed later). $E^{\pm}_{ijk}$ stands for an intrinsic activation energy: it should be in principle local similarly to k_{ijk}, but at this stage we choose to assume it is not affected by coke and sulfides deposits. The same is assumed for $K^{\mathrm{ads}}_{\mathrm{A}2k}$ the adsorption constants of asphaltenes of type ''2'' with respect to the catalyst surface. However, these latter parameters depend, according to the Boltzmann equation, exponentially on the inverse of temperature. Finally, C^{l}_{ij} stands for the local concentration of reactant ij in liquid phase l.

Next, the Fick law is assumed to describe correctly the intragranular mass transfer:

$$N^{\mathrm{l}}_{ijk}(r,z,t) = -D^{\mathrm{eff}}_{ijk}(r,z,t)\mathrm{grad}[C^{\mathrm{l}}_{ij}(r,z,t)] \quad (2)$$

where the D^{eff}_{ijk} are the local effective diffusion coefficients, which basically depend on temperature and the local textural properties, as also described below. The mass balance around an element of catalytic volume connects as usual Eqs. (1) and (2):

$$\mathrm{Div}(N^{\mathrm{l}}_{ijk}(r,z,t)) = -\rho_{ijk}(r,z,t) \quad (3)$$

where the $N^{\mathrm{l}}_{ijk}(r,z,t)$ are the local molar fluxes in liquid phase.

The deposition of (Ni, V) sulfides particles inside the catalysts pore space is known to proceed through a nucleation and growth mechanism [2,3], with nucleation centers homogeneously distributed across the porous medium, and a radial distribution of sizes in correspondence with the average distribution measured by for instance a X-ray microprobe since these sizes are much smaller than the sampling volume. We represent this distribution as an homogenized local concentration of metals (Ni, V) in solid phase $C^{\mathrm{s}}_{\mathrm{m}}(r,z,t)$ with:

$$\frac{\mathrm{d}C^{\mathrm{s}}_{\mathrm{m}}(r,z,t)}{\mathrm{d}t} = \frac{M_{\mathrm{m}}}{d^0_{\mathrm{g}}}\sum_j \rho_{\mathrm{m}j}(r,z,t) \tag{4}$$

where M_{m} is the average molar mass of metals and d^0_{g} the initial grain density of the catalyst (indexed by k, according to the interval of z).

Coke deposition is assumed to result from a reversible reaction of dehydrogenation of asphaltenic material, and its rate to be first-order with respect to a driving force equal to the difference between actual $C^{\mathrm{s}}_{\mathrm{coke}}(r,z,t)$ and equilibrium $C^{\mathrm{s}^*}_{\mathrm{coke}}(r,z,t)$ local coke concentrations in solid phase:

$$\frac{\mathrm{d}C^{\mathrm{s}}_{\mathrm{coke}}(r,z,t)}{\mathrm{d}t} = k_{\mathrm{coke},k}(r,z,t)S_k(r,z,t)\exp\left(\frac{E^{\pm}_{\mathrm{coke},k}}{RT}\right) \times \left[C^{\mathrm{s}^*}_{\mathrm{coke}}(r,z,t) - C^{\mathrm{s}}_{\mathrm{coke}}(r,z,t)\right] \tag{5}$$

The coke forming equilibrated reaction can be schematized as:

$$\mathrm{Asphaltene(liquid\ phase)} \Leftrightarrow \mathrm{Coke(solid\ phase)} + n\mathrm{H_2(gas\ phase)}\,\Delta G^0_{\mathrm{coke}}$$

So that, following the law of mass action, the equilibrium local coke concentration can be expressed as:

$$C^{\mathrm{s}^*}_{\mathrm{coke}}(r,z,t) = P^{-n}_{\mathrm{H_2}}\exp\left(\frac{-\Delta G^0_{\mathrm{coke}}}{RT}\right)C^{\mathrm{l}}_{\mathrm{Asph},1}(r,z,t) \tag{6}$$

where $P_{\mathrm{H_2}}$ is the partial pressure of hydrogen in gas phase, and $\Delta G^0_{\mathrm{coke}}$ characterizes the feedstock.

It is known that initial coke deposit strongly reduces the initial activities, while the poisoning is less marked as coke further accumulates [4]. To account for this non linear deactivation effect of coke, the model assumes the following relationship between local intrinsinc rate constants and local coke concentrations:

$$k_{ijk}(r,z,t) = k^0_{ijk}\left[1 + \frac{C^{\mathrm{s}}_{\mathrm{coke}}(r,z,t)}{C^{\mathrm{s}^*}_{\mathrm{coke}}(r,z,t)}\right]^{-4} \tag{7}$$

The local effective diffusivities $D^{\mathrm{eff}}_{ijk}(r,z,t)$ in (2) play a central role in determining the magnitude of intragranular concentration gradients. For the time being, we assume they are proportional to the molecular diffusivities D^{m}_{ij} and to some function $g(\varepsilon)$ of the local catalyst void fraction:

$$D^{\mathrm{eff}}_{ijk}(r,z,t) = D^{\mathrm{m}}_{ij}(z,t)g[\varepsilon_k(r,z,t)] \tag{8}$$

We relate the molecular diffusivities to the liquid phase viscosity ν, to the radius of gyration r^{g}_{ij} of the diffusing species, and to temperature through the Stokes–Einstein law:

$$D^{\mathrm{m}}_{ij}(z,t) = \frac{RT(z,t)}{[6\pi\nu r^{\mathrm{g}}_{ij}(z,t)]} \tag{9}$$

The law of Andrade specifies the variation of the feed viscosity with temperature, so that we derive the following temperature dependence for molecular diffusivities:

$$D^{\mathrm{m}}_{ij}(z,t) = D^{0\mathrm{m}}_{ij}\frac{T(z,t)}{T_0}\exp\left(\frac{E^{\pm\mathrm{diff}}_{ij}}{R}\left(\frac{1}{T(z,t)} - \frac{1}{T_0}\right)\right) \tag{10}$$

In Eq. (10), notice that we have introduced the assumption that catalyst grains remain always isothermal everywhere, so that temperature remains a function of longitudinal position z and time only. In this equation, two new parameters are introduced: a temperature of reference T_0 (in Kelvin), at which the molecular diffusivity of reference $D^{0\mathrm{m}}_{ij}$ is measured, and an energy of activation of molecular diffusivity, $E^{\pm\mathrm{diff}}_{ij}$, (in cal mol^{-1} if the ideal gas constant R is given in cal mol^{-1} K^{-1}).

In Eq. (9) we use the radii of gyration r^{g}_{ij}, but it is more convenient to relate these to molecular weights M_{ij} which usually are the primary analytical data available for entities like asphaltenes or resins in resids and heavy crudes. To do this, one can transpose from the theory of polymer solutions a power law of the type:

$$r^{\mathrm{g}}_{ij} = K_{ij}M^{1/d_{\mathrm{F}}}_{ij} \tag{11}$$

We have adopted the value 1/3 for the exponent $1/d_{\mathrm{F}}$. In Eq. (11), since asphaltenes and resins in hydrocarbon solutions behave as fractal objects with a fractal dimension d_{F} close to 3 [5]. Let us now return to the representation of the influence of the local textural properties on the effective diffusivities. In the present version of THERMIDOR, we start with the classical expression introducing a local tortuosity factor τ [6], further corrected by Spry and Sawyer in order to account for hindered configurational diffusion of large supramolecular entities like asphaltenes, resins and metal bearing complexes in resids [7]:

$$g[\varepsilon_k(r,z,t)] = \frac{\varepsilon_k(z,r,t)}{\tau_k(z,r,t)}[1 - \lambda_{ijk}(r,z,t)]^4 \tag{12}$$

In Eq. (12), the quantity λ_{ijk} is following Spry and Sawyer, the ratio of radius of gyration over radius of pores, assuming for the latter that a single mode is involved in mass transfer:

$$\lambda_{ijk} = \frac{r^{\mathrm{g}}_{ij}}{r^{\mathrm{pores}}_k(r,z,t)} \tag{13}$$

For the local tortuosity factor, we assume the validity of the upper bound correlation given by [8] for a packing of random spheres:

$$\tau_k^{-1}(r,z,t) = \left(\frac{\varepsilon_k(r,z,t)}{1-\frac{1}{2}\log(\varepsilon_k(r,z,t))}\right) \quad (14)$$

Finally, inserting Eqs. (10)–(14) into Eq. (8), we arrive at an expression where the local mass transfer coefficient $D_{ijk}^{\text{eff}}(r,z,t)$ depends solely on the local porosity $\varepsilon_k(r,z,t)$ and the local average pore radius $r_k^{\text{pores}}(r,z,t)$. It remains to specify how both quantities vary with the amount of metal sulfides and coke deposited locally as solid reaction products.

2.1.3. Representation of catalytic porous media

Here, we have used extensions of the Random Spheres Model (RSM) [8,9] to Random Needles (RNM) and Random Coins (RCM), as introduced by Macé and Wei [10] some time ago: this explains our choice of Eq. (14). In the RSM, spheres of radius b and volumic density n^{s} are placed at random in space, and allowed to overlap. The RCM is derived from the RSM by cutting off from each sphere the parts outside two parallel planes each placed at a distance e from the sphere center and oriented at random. The RNM is derived from the RSM by keeping from each sphere the part inside a cylinder of radius e, the principal axis of which passes through the sphere center and is oriented at random. For the three types of media, with α the aspect ratio b/e, the general results for the porosity ε and the surface area Σ are [10]:

$$\varepsilon = \exp\left[-\left(\frac{4\pi}{3}\right)n^{\text{s}}\beta\left(\frac{b}{\alpha}\right)^3\right] \quad (15)$$

$$\Sigma = 4\pi n^{\text{s}}\xi\left(\frac{b}{\alpha}\right)^2\varepsilon \quad (16)$$

where β and ξ are shape factors depending solely on α. They are equal to 1 in the RSM.

For random coins:

$$\beta_{\text{coin}} = 1 + 3\int_1^{\alpha} r^2 \ln\left(\frac{r}{r-1}\right)\mathrm{d}r \quad (17)$$

$$\xi_{\text{coin}} = \alpha + \frac{1}{2}(\alpha^2 - 1) \quad (18)$$

For random needles:

$$\beta_{\text{needle}} = 1 + 3\int_1^{\alpha} r^2 \ln\left(\frac{r}{\sqrt{r^2-1}}\right)\mathrm{d}r \quad (19)$$

$$\xi_{\text{needle}} = \alpha^2 + (1-\alpha)\sqrt{\alpha^2-1} \quad (20)$$

Moreover, a good estimate of the corresponding equivalent pore diameter is given by the formula:

$$r^{\text{pores}} = \frac{4\varepsilon}{\Sigma} \quad (21)$$

These models are suitable to represent the fresh catalysts as random porous media, but moreover, they are very convenient to account for the catalyst ageing resulting from the nucleation and homothetic growth of solid deposits (metal sulfides and coke) inside the porosity. Indeed, the aged catalyst may be represented by the superposition of three random media according to Fig. 2: the fresh catalyst, the metal sulfides deposit and the coke deposit, and it is straightforward to derive exact relationships relating the residual porosity, surface area, coke volume and metal sulfide deposit volume to the dimensions and aspect ratios of the constitutive elementary particles for each random distribution. With indices F, M and C, respectively, for the fresh porous medium, the porous medium formed by the spatial distribution of metal sulfides particles, and the porous medium formed by the spatial distribution of coke particles, we write:

$$\varepsilon_k(r,z,t) = [\varepsilon_{k\text{F}} - V_{k\text{M}}(r,z,t) - V_{k\text{C}}(r,z,t)] \quad (22)$$

where $V_{k\text{M}}$ and $V_{k\text{C}}$ are the local volume fractions of metal sulfides and coke accumulated at time t. In addition, one has:

$$\varepsilon_k(r,z,t) = \exp\left[\left(\frac{-4\pi}{3}\right)\left(n_{k\text{F}}^{\text{s}}\beta_{k\text{F}}\left(\frac{b_{k\text{F}}}{\alpha_{k\text{F}}}\right)^3 + n_{k\text{M}}^{\text{s}}\beta_{k\text{M}}\left(\frac{b_{k\text{M}}(r,z,t)}{\alpha_{k\text{M}}}\right)^3 + n_{k\text{C}}^{\text{s}}\beta_{k\text{C}}\left(\frac{b_{k\text{C}}(r,z,t)}{\alpha_{k\text{C}}}\right)^3\right)\right] \quad (23)$$

The probabilities P_{ki} that a point belongs to a solid particle if the distributions of fresh catalyst, metal sulfides and coke are separated in space are equal to $(1-\varepsilon_{ki})$, with i = F, M, C:

$$P_{ki}(r,z,t) = 1 - \exp\left[\left(\frac{-4\pi}{3}\right)n_{ki}^{\text{s}}\beta_{ki}\left(\frac{b_{ki}(r,z,t)}{\alpha_{ki}}\right)^3\right] \quad (24)$$

Considering that the fresh catalyst exists prior to deposits, and that a deposit is either coke or metal sulfides, we arrive at the following relationships by the proper combination of independent probabilities:

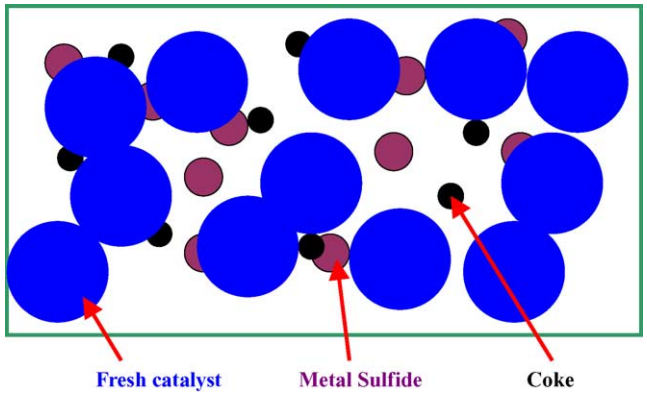

Fig. 2. Schematic representation of an aged catalyst as the superposition of three random porous media: fresh solid + metal sulfides deposit + coke.

$$V_{k\mathrm{M}} = P_{k\mathrm{M}} - P_{k\mathrm{F}}P_{k\mathrm{M}} - \frac{1}{2}(P_{k\mathrm{M}}P_{k\mathrm{C}}) + \frac{1}{2}(P_{k\mathrm{F}}P_{k\mathrm{M}}P_{k\mathrm{s}}) \quad (25)$$

$$V_{k\mathrm{C}} = P_{k\mathrm{C}} - P_{k\mathrm{F}}P_{k\mathrm{C}} - \frac{1}{2}(P_{k\mathrm{M}}P_{k\mathrm{C}}) + \frac{1}{2}(P_{k\mathrm{F}}P_{k\mathrm{M}}P_{k\mathrm{C}}) \quad (26)$$

$V_{k\mathrm{M}}(r,z,t)$ and $V_{k\mathrm{C}}(r,z,t)$ are directly proportional to the concentrations in solid phase $C^{\mathrm{s}}_{\mathrm{m}}(r,z,t)$ and $C^{\mathrm{s}}_{\mathrm{coke}}(r,z,t)$, respectively, determined by Eqs. (4) and (5). The unknown $b_{ki}(r,z,t)$ (i = M, C) are therefore determined as solutions of the system (24)–(26), allowing to determine local residual surface areas and pore sizes, for which exact expressions were derived in a similar way as for (25) and (26).

THERMIDOR has been designed to represent the broadest possible family of hydrotreating catalysts, including naturally the macroporous kind, and in particular, the ''chesnut bur'' proprietary HDM catalyst [11].

In the general case, the presence of macropores is accounted for by considering the solid as made of randomly seeded macrodomains (spheres, coins or needles but usually spheres), i.e. of typical size of the order of a few microns, leaving void interstices representing the macropores. These macrodomains embed random seeds of nano-particles (again, spheres, needles or coins, but coins are the most suited for representing the platelets of gamma alumina almost exclusively used to manufacture standard hydrotreating catalysts). The texture of a fresh macroporous catalyst can then be determined by 6 parameters at most: $b_{\mathrm{F}i}$, $\alpha_{\mathrm{F}i}$, $n^{\mathrm{s}}_{\mathrm{F}i}$ where the index i = 1 or 2 now stands for macropores or mesopores. We decide first the shapes of objects (spheres, needles, or coins) and their aspect ratios $\alpha_{\mathrm{F}i}$: for that, electron microscopy studies of the real fresh catalysts and a good knowledge of the manufacturing process may be helpful. The remaining four parameters can be determined by calibration using measured textural properties of the real catalyst: macropores and mesopores volumes, and average macropores radii can be determined for instance from mercury porosimetry data, and specific area by the BET method. A check of consistency can then be provided by the comparison of predicted (from Eq. (20)) and measured (by mercury porosimetry) average mesopore radii. THERMIDOR includes identification routines so that experimental textural data can be input directly. Of course, in the case of monomodal catalysts, it suffices to identify 2 parameters, e.g. total pore volume and surface area, after the aspect ratio has been chosen.

The ''chesnut bur'' catalysts receive a special treatment: the spherical macrodomains of radius b_{Fmacro} are now the ''burs'' themselves. For each of these domains the radial organisation of acicular alumina platelets is approximated by considering that at any fractional radius $x = b/b_{\mathrm{Fmacro}}$ inside the sphere, the cross-section of these platelets by the corresponding spherical envelope forms a bi-dimensional random needle model (2D RNM), as represented in Fig. 3. The average number of acicular platelets per spherical macrodomain being fixed, the areal density of 2D needles is now decreasing with increasing fractional radius. In this case, the identification strategy starts by an estimation of the chesnut bur average radius b_{Fmacro}, using for instance SEM micrographs as presented in Fig. 4. In

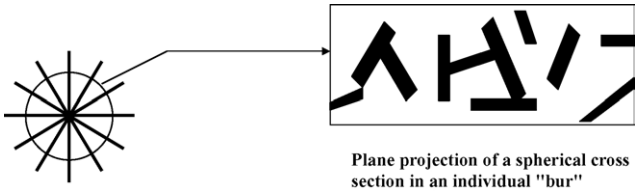

Fig. 3. Schematic representation of burs in the ''chesnut bur'' multimodal catalyst: inside a spherical bur, a cross-section of the radially oriented acicular alumina platelets by any concentric spherical envelope forms a bi-dimensional random needle model (2D RNM).

view of their particular manufacturing process [11] we assume the burs do not interpenetrate. The effective number of burs per unit volume $n^{\mathrm{eff}}_{\mathrm{Fmacro}}$ is then evaluated according to:

$$n^{\mathrm{eff}}_{\mathrm{Fmacro}} = \frac{1 - \varepsilon_{\mathrm{Fmacro}}}{\frac{4\pi}{3} b^3_{\mathrm{Fmacro}}} \quad (27)$$

with $\varepsilon_{\mathrm{Fmacro}}$ the experimental macropore volume as determined by mercury porosimetry. The complement to the experimental total pore volume, $\varepsilon_{\mathrm{Fmeso}}$, is assigned to mesopores, and the volume of platelets per single chesnut bur is now:

$$V_{\mathrm{platelets}} = \left[\frac{4}{3}\pi b^3_{\mathrm{Fmacro}} - \frac{\varepsilon_{\mathrm{Fmeso}}}{n^{\mathrm{eff}}_{\mathrm{Fmacro}}}\right] \quad (28)$$

The total area developed by acicular platelets per single chesnut bur is simply:

$$S_{\mathrm{platelets}} = \frac{S_{\mathrm{Ftotal}}}{n^{\mathrm{eff}}_{\mathrm{Fmacro}}} \quad (29)$$

In the 2D RNM, the specific area $\varepsilon_{2\mathrm{D}}$ and specific perimeter $\Sigma_{2\mathrm{D}}$ have expressions analogous to 3D Eqs. (15) and (16) but in 2D. With the aspect ratio α_{Fmeso} of 2D needles estimated for instance from TEM micrographs, the remaining unknowns are the number of platelets per bur $n^{\mathrm{s}}_{\mathrm{Fmeso}}$ and the half-length of a 2D needle b_{Fmeso}. They will be identified thanks to the following integrals, making use of the results of Eqs. (28) and (29):

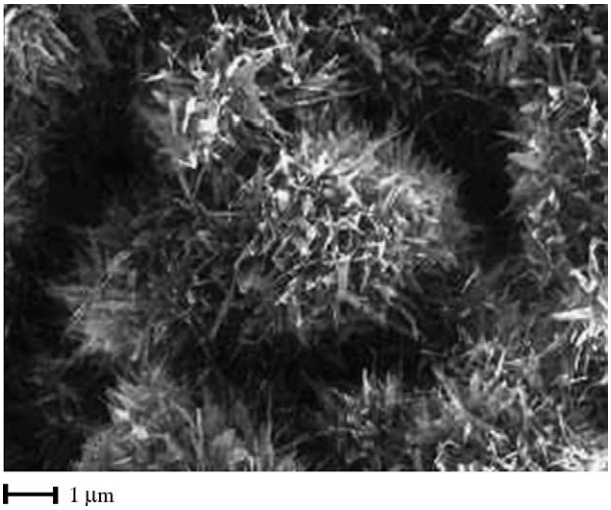

Fig. 4. Scanning electron microscopy picture of the ''chestnut bur'' porous structure characteristic of the HDM catalyst A.

$$V_{\text{platelets}} = 4\pi \int_0^{b_{\text{Fmacro}}} \left[1 - \exp\left(\frac{-C_1}{x^2}\right)\right] x^2 \, \mathrm{d}x \tag{30}$$

$$S_{\text{platelets}} = C_2 \int_0^{b_{\text{Fmacro}}} \exp\left(\frac{-C_1}{x^2}\right) \mathrm{d}x \tag{31}$$

where C_1 and C_2 are constants defined by:

$$C_1 = \frac{1}{4} n^{\text{s}}_{\text{Fmeso}} \beta_{\text{2DRN}} \left(\frac{b_{\text{Fmeso}}}{\alpha_{\text{Fmeso}}}\right)^2 \tag{32}$$

$$C_2 = 2\pi n^{\text{s}}_{\text{Fmeso}} \xi_{\text{2DRN}} \left(\frac{b_{\text{Fmeso}}}{\alpha_{\text{Fmeso}}}\right) \tag{33}$$

and the shape factors for 2D RNM are:

$$\beta_{\text{2DRN}} = 1 - \int_1^{\alpha_{\text{F,meso}}} 2x \ln\left[1 - \frac{2}{\pi} \arccos\left(\frac{\sqrt{x^2 - 1}}{x}\right)\right] \mathrm{d}x \tag{34}$$

$$\xi_{\text{2DRN}} = \frac{2}{\pi}\left[\sqrt{\alpha^2_{\text{Fmeso}} - 1} + \alpha_{\text{Fmeso}} \arcsin\left(\frac{1}{\alpha_{\text{Fmeso}}}\right)\right] \tag{35}$$

In practice, C_1 is deduced from (30) by numerical inversion (Newton method), then C_2 is determined from (31), and the unknowns are derived as solutions of the system formed by Eqs. (32) and (33). Lastly, the average mesopore radius r_{Fmeso} is determined by averaging the hole radius $r_{\text{2DRN}}(x)$ along the radius of one bur, with:

$$r_{\text{2DRN}}(x) = \frac{4x^2}{n^{\text{s}}_{\text{Fmeso}} b_{\text{Fmeso}} \xi_{\text{2DRN}}} \tag{36}$$

$$r_{\text{Fmeso}} = \frac{3}{2\pi r^3_{\text{Fmacro}}} \int_0^{r_{\text{Fmacro}}} 4\pi r_{\text{2DRN}}(x) x^2 \, \mathrm{d}x \tag{37}$$

Finally:

$$r_{\text{Fmeso}} = \frac{24 r^2_{\text{Fmacro}}}{5 n^{\text{s}}_{\text{Fmeso}} b_{\text{Fmeso}} \xi_{\text{2DRN}}} \tag{38}$$

For this particular chesnut bur geometry, the nucleation and growth of metal sulfides and coke particles are treated similarly as for the other less complex RSM, RCM or RNM geometries, and one arrives at equations similar to (22)–(26) for the local residual pore volume, surface area and mesopore radius.

Another crucial feature in THERMIDOR is the introduction of a percolation threshold for the residual local pore space, below which it becomes locally discontinuous, and mass transfer is interrupted. In principle this threshold depends on the radius of gyration of molecules transported, since bigger molecules explore only a subset of the pore space accessible to smaller molecules. As coke and metal sulfides are laid down, the local pore space and mesopore radius decrease. Mass transfer may be discontinued for a molecular species of given radius of gyration, either when the residual pore space becomes locally lower than the percolation threshold for the considered medium, or when the local pore radius becomes smaller than the radius of gyration times some coefficient. These conditions are tested locally at every time step in THERMIDOR, so as to determine where and when pore occlusion occurs for each reactant considered in the simulation. For instance, in the case of a strong radial concentration gradient determined by significant diffusional limitations in a particular type of catalyst pellet, pore mouth plugging will occur early in the life of this catalyst, first selectively for the larger reactants, then completely when shutdown occurs also for diffusion of the smallest.

2.1.4. Heat balances

Since the goal of THERMIDOR is to simulate industrial operations, which are run in adiabatic large scale reactors, it is necessary to couple heat balances and mass balances so as to compute $T(z,t)$, the longitudinal temperature profile. We assume a perfect piston flow for each trickle bed, which implies perfect radial mixing. The examination of radial temperature profiles records from industrial units confirms a posteriori the validity of this assumption.

The heat balance equation in THERMIDOR assumes a pseudo steady state, thermal equilibrium between solid, liquid and gas phases at any position z and any time t, and heat transfer solely by convection through the liquid. The following differential equation can be derived:

$$\frac{\mathrm{d}T(z,t)}{\mathrm{d}z} = \frac{[1 - \phi_{\text{ext}}(z)] \sum_{ij} N^{\text{l}}_{ijk}(r^{\text{g}}_k z, t) \Delta H_{ij}}{\text{LHSV}(C + F)} \tag{39}$$

with $\phi_{\text{ext}}(z)$ the extra-granular void fraction (assumed constant along each bed of catalyst), the $N^{\text{l}}_{ijk}(r^{\text{g}}_k, z, t)$ the fluxes of reactants consumed by each grain of catalyst k at the location z and time t, and ΔH_{ij} the heats of reaction (counted positive for an exothermic reaction, the sum being in principle algebraic). C is the local heat capacity, and F the local heat capacity flux:

$$C = \phi_{\text{ext}}(z)[(1 - Y) c^{\text{l}}_{\text{p}} d^{\text{l}} + Y c^{\text{g}}_{\text{p}} d^{\text{g}}] + (1 - \phi_{\text{ext}}) c^{\text{s}}_{\text{p}} d^{\text{s}} \tag{40}$$

$$F = c^{\text{l}}_{\text{p}} d^{\text{l}} + \frac{Q^{\text{g}}}{Q^{\text{l}}} c^{\text{g}}_{\text{p}} d^{\text{g}} \tag{41}$$

where Y is the local fraction of gas in the extra-granular space, the c^i_{p} the specific heats and d^i the densities for liquid (i = l), gas (i = g) and solid (i = s) phases. The c^i_{p} and d^i are assumed temperature dependent only for the liquid and gas phase. In other terms, the composition of the liquid phase and the gas phases are assumed to vary only slightly along the reactors, since hydrotreating affects marginally the feedstock chemistry, and the high linear velocity of gas tends to minimize composition gradients (mostly H_2S content) along the reactors. Q^{g} and Q^{l} are the flow rates of gas and liquid, assumed constant in reaction sections separated by quenches (see below). We use for c^{l}_{p} the correlation provided by Perry [12] for hydrocarbon oils:

$$c^{\text{l}}_{\text{p}} = \frac{\alpha^{\text{l}}}{\sqrt{d^{\text{l}}}} + \beta^{\text{l}}(T - 288) \tag{42}$$

with $\alpha^{l} = 0.415$ kcal g^{-1} K^{-1} and $\beta^{l} = 9 \times 10^{-4}$ kcal g^{-1} K^{-2}. For c_p^g, we retain the formula for an ideal gas. The c_p^s and d_p^s are local since they depend on the amount of metal sulfides and coke laid down, and also as a consequence on the amount of liquid filled residual grain porosity at z and t. These quantities can be obtained by averaging (r,z,t) dependant quantities furnished by the description at the grain scale. We assume a linear dependency of c_p^s on the specific heats of metal sulfides, coke and fresh catalysts, themselves assumed to depend linearly on temperature.

In HYVAHL industrial units, like in many hydroconversion units involving catalytic beds and reactors in series, temperatures are moderated by the use of ''quenches'', that is to say devices where relatively cold hydrogen is injected and well mixed to the gas–liquid mixture collected at a bed or reactor outlet. The utility of quenches is two-fold: (i) to limit temperature elevation due to the heat released by the globally exothermal hydrotreating reactions and (ii) to adjust the hydrogen partial pressure to compensate for the hydrogen consumed and the amount of H_2S and hydrocarbon gases released at the previous stage. $T(z,t)$ has therefore a saw teeth profile. If a multi-bed multi-reactor HYVAHL unit is to be simulated, it is quite important to determine correctly the inlet temperature T_{inlet}^{q+1} resulting from the quenching processes at quench q, following reactor q. This temperature is the positive solution of the parabolic equation which results from solving mass and heat balances around the quench:

$$A_2(T_{\text{inlet}}^{q+1})^2 + A_1(T_{\text{inlet}}^{q+1}) + A_0 = 0 \tag{43}$$

with coefficients:

$$A_2 = \beta^{l} d^{l} \tag{44}$$

$$A_1 = \left[\frac{\alpha^{l}}{\sqrt{d^{l}}} - 288\beta^{l}\right] d^{l} + [G_{\text{outlet}}^{q} + G_{H_2}^{q}] d^{g} c_p^{g} \tag{45}$$

$$A_0 = -[d^{l} c_p^{l}(T_{\text{outlet}}^{q}) T_{\text{outlet}}^{q} + G_{\text{outlet}}^{q} d^{g} c_p^{g} T_{\text{outlet}}^{q} + G_{H_2}^{q} d^{g} c_p^{g} T_{H_2}^{q}] \tag{46}$$

In these equations, G_{outlet}^{q} and $G_{H_2}^{q}$ are the ratios of gas flow rates to the liquid flow rate, expressed in standard cubic meter per cubic meter, respectively, of process gas at the outlet of reactor q, and fresh gas admitted at quench q.

2.1.5. About pressure drop

For the time being, we neglect the longitudinal variation of partial pressures in the gas phase, and we do not attempt to solve the momentum balance so as to derive the total pressure profile. This feature would be, however, useful as the total pressure drop across the unit should not exceed a threshold determined mainly by the capacity of the recycle compressor. It is observed that pressure drop increases faster across the first guard bed, due to the deposition of sediments and furnace tubes corrosion products (iron sulfide scales) which block partly the interstitial voids between catalyst grains. The damage is accentuated by extra coking around these fines. A proper use of specially designed guard material, and a good catalyst loading scheme, limit the phenomenon to some extent. The Permutable Reactor System (PRS) technology, implemented by AXENS in HYVAHL industrial units, is another efficient way to tackle this scale induced pressure drop problem. However, the catalyst activity for spilling over activated hydrogen (beneficial) or activated coke precursors (detrimental) is very important as well. The amount of coke laid down inside the catalyst grains is an excellent indicator of this. It has been until now a distinctive feature of the chesnut bur type catalysts to show a relatively low coking propensity compared to their competitors, and it has been verified industrially several times that accordingly pressure drop build-up is slower when guard beds are loaded with such materials. Understanding pressure drop changes in the HYVAHL process is a subject of active research and will hopefully result in new simulation routines implemented in future versions of THERMIDOR.

2.1.6. Simulation algorithm

An overview of the simulation algorithm is necessary to understand properly the scope and objectives of THERMIDOR: the following check-list defines the sequence of inputs to be provided by the user:

1. Choose the type of reactor between adiabatic and isothermal.
2. If adiabatic, choose the concentration C^{l*} of a component (a particular sub species or a lump of sub species, e.g. sulfur compounds) to be maintained constant in the effluent, the conversion level (e.g.: sulfur, 92%), and the maximum temperature acceptable in the reactor $T_{\max}$. The latter will set a limit to the simulated run.
3. If isothermal, choose the operating temperature.
4. Define the global liquid hourly space velocity (LHSV), average total pressure, make up and recycle gas ratios and Y the fraction of gas.
5. Define the feedstocks in terms of the np pseudo-constituents, their initial concentrations C_{ij}^{l0}, molecular weights M_{ij}, reference molecular diffusivities D_{ij}^{0m}, activation energy for diffusion $E_{ij}^{\pm\text{diff}}$ and reference temperature T_0, heats of reaction ΔH_{ij} and the standard enthalpy and equilibrium constant of coking $\Delta H_{\text{coke}}^{\circ}$ and K_{coke}.
6. Define the discretisation intervals in space (z and r) and time, and the maximum duration of the simulation.
7. Define the number of catalytic beds associated in series and the corresponding fractions of the total catalytic volume.
8. Specify for each bed the catalyst and its characteristics.
9. Specify for each bed the number of quenches, their position in z, and the corresponding quench gas to liquid ratios $G_{H_2}^{q}$, and $T_{H_2}^{q}$ the temperatures of quench gases.
10. Define the nature and number of output charts and data files.
11. Run the simulation.

For each catalyst k are specified its shape (cylinder or spheres), pellet radius r_k^g, grain density and loading density, textural parameters and kinetic parameters. The textural parameters depend on the representation chosen. For instance, for a monomodal mesoporous catalyst (e.g. second stage HDS catalyst) the user chooses the type of model (RSM, RCM or

RNM) for the fresh catalyst, the metal sulfides and the coke deposits, and the corresponding aspect ratios. He is then prompted for the experimental characteristics required for the identification, in that case, total pore volume and specific area, and optionally the experimental average mesopore radius for a check. For bimodal or chesnut bur catalysts, the necessary additional experimental input is required. The kinetic parameters consist of the set of initial intrinsic rate constants k^0_{ijk} and activation energies $E^{\pm ij}_k$, the adsorption constants of "type 2" asphaltenes $K^{0\text{ads}}_{\text{A2}k}$ and the associated enthalpies of adsorption $\Delta H^{\text{ads}}_{\text{A2}k}$, and finally, for the coking reaction, the intrinsic rate constant $k_{\text{coke},k}$, and the energy of activation $E^{\pm}_{\text{coke},k}$. The other parameters which in principle are independent of the feedstock or catalysts are specified in a separate file (percolation threshold, densities of solids, etc...).

The first stage, once the simulation is launched, for instance in the adiabatic case, is the identification of the catalysts textural parameters according to the chosen model representations. A specific output file is generated with the results, allowing a posteriori checks of consistency. Next, the temperature $T(z,0)$ and concentration $C^{\text{l}}_{ij}(r,z,0)$ fields at time 0 are determined, using an iterative search for the solution of Eqs. (1), (2) and (39), (43) under the constraint C^{l^*} at outlet. A simple finite difference scheme is implemented to solve numerically the set of coupled equations. Eqs. (4) and (5) are then solved to determine the distributions $C^{\text{s}}_{\text{m}}(r,z,\Delta t)$ of metal sulfides and $C^{\text{s}}_{\text{coke}}(r,z,\Delta t)$ of coke deposited after the first increment of time. This allows the textural parameters (and therefore the effective diffusion coefficients), and kinetic parameters of catalysts to be updated at every grid point in r and z. The temperature and concentration fields are then updated, to give $T(z,\Delta t)$ and $C^{\text{l}}_{ij}(r,z,\Delta t)$, new solutions of the problem C^{l^*} at outlet. The algorithm is iterated until $T_{\max}$ is reached at some z, or the maximum duration (number of time increments allowed) is reached. Output data files are generated at the specified time intervals, for post-run analysis. THERMIDOR was originally written in FORTRAN 77 language. It comprises about 5000 lines of code. One simulation takes typically 1 to a few hours on a PC equipped with a Pentium III.

2.2. Experiments

2.2.1. Choice and characterization of catalysts

Catalysts with various textural parameters have been selected to validate the different models of catalysts which are introduced in THERMIDOR.

In this study, the results of this validation on two catalysts are reported. The pore distributions and the chemical and physical properties of both catalysts are presented in Fig. 5 and Table 1, respectively. These two catalysts are extremely different in shape, in size of grain, in pore distribution and in pore structure.

A is a high capacity $NiMo/Al_2O_3$ HDM catalyst which is characterized by a multi-modal pore distribution. The key to its high capacity is a "chestnut bur" pore structure. This type of structure (Fig. 4) is specially designed to increase the accessibility of the large molecules. The macroporosity, which is provided by the interstices between the burs, allows asphaltenes and resins to move quickly through the grain mass and to access to a maximum of active surface. The active surface is in the mesoporosity of alumina acicular platelets which are agglomerated in the "chestnut bur" structure. This type of structure is characterized by a continuous pore distribution between macropores and mesopores (Fig. 5). A high metal retention capacity, up to 100 g (Ni + V)/100 g of fresh catalyst, is reached depending on the feed and operating conditions as well as process objectives. The metal retention capacities of the conventional macroporous structures are significantly lower. These structures are indeed generally formed by the agglomeration of mesoporous alumina particles and the macroporosity results from the inter-particle free spaces.

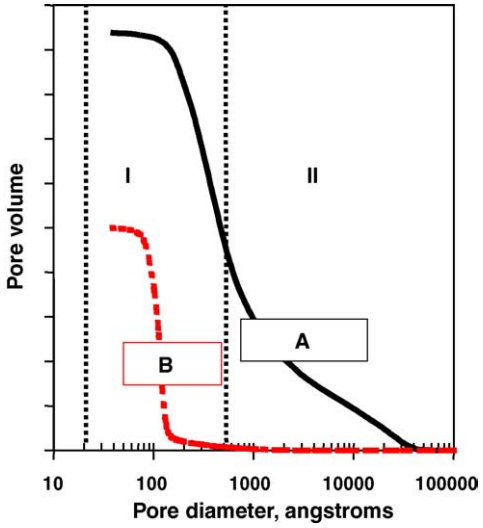

Fig. 5. Pore size distributions of HDM (A) and HDS (B) catalysts as revealed by high pressure mercury prosimetry (I: range of mesopores, II: range of macropores).

B is a $CoMo/Al_2O_3$ HDS catalyst which is characterized by a mesoporous monomodal pore distribution. This type of porosity results from a compact agglomeration of mesoporous alumina particles. The metal retention capacity of this catalyst can only reach 10 g (Ni + V)/100 g of fresh catalyst.

2.2.2. Catalytic tests

Catalytic tests were run on a bench scale unit which was equipped of an up-flow trickle-bed tubular reactor. After the in situ sulfiding of the catalyst, the test procedure consists of two steps:

1. The first step allows us to determine the initial performances in HDM and HDS on an Arabian Light Atmospheric Residue (ALAR) that contains low amounts of metals.

Table 1
Chemical and physical properties of catalysts

	HDM catalyst A	HDS catalyst B
Shape	Spherical	Cylindrical
Size (mm)	1.4–2.8	1.2
Active phase	NiMo	CoMo
Surface area ($cm^2\ cm^{-3}$)	0.952×10^6	2.852×10^6
Pore volume ($cm^3\ cm^{-3}$)	0.768	0.639

Table 2
Characterization of feedstocks

	Arabian light atmospheric residue (ALAR)	Boscan crude petroleum (BCP)	Industrial unit vacuum residue (VR)[a]
Density (g cm^{-3})	0.96	1.010	0.993
Viscosity at 100 °C (cSt)	25.6	230	119
Sulfur (wt%)	3.34	5.28	3.5
Nitrogen (wt%)	0.21	0.67	–
Ni (ppm)	9	196	17
V (ppm)	38	1150	72
Asphaltenes[b] (wt%)	3.1	13.0	5.7
CCR[c] (wt%)	9.5	12.0	17.1

[a] Averages.
[b] Insolubles in *n*C7.
[c] Conradson carbon residue.

2. The second step allows us to characterize the evolution of HDM and HDS performances versus time-on-stream using a feedstock very rich in metals (Boscan Crude Petroleum). This feed is injected until complete deactivation of the catalyst, that is to say, until the thermal conversion corresponding to a level of 20% for HDM and a level of 10% for HDS in the test conditions is observed. This second step is a rapid aging test which allows us to evaluate a metal retention capacity.

The characteristics of feedstocks and the experimental conditions are presented in Tables 2 and 3, respectively.

In practice, a volume of 40 cm^3 of undiluted catalyst was loaded in a rigorously isothermal zone of the reactor. After loading, the catalyst was in situ sulfided with a straight run gas oil doped with 2 wt% dimethyl disulfide in the conditions given in Table 3. After sulfiding, the catalyst was cooled down to 150 °C and the sulfiding feed was stopped. The ALAR feedstock was introduced and the conditions were adjusted to the desired start-of-run conditions. After 300 h under ALAR, the temperature was decreased down to 150 °C and the BCP feedstock was introduced. The temperature was increased up to 390 °C and the conditions were kept isothermal until complete deactivation of the catalyst. The products were collected every 12 h and metals and sulfur were analyzed by X-ray fluorescence.

2.2.3. Industrial run

Data were collected from a recent 317 days cycle of operations of a typical HYVAHL unit, denoted cycle C below. We concentrated on the first part of this cycle, which lasted 72 days before reactors R1A and R1B were switched using the PRS system. Industrial HDM and HDS catalysts were provided by AXENS. These catalysts are comparable to A and B. The HDM catalyst was dense loaded in R1A, R1B and R2, representing about 40% of the total catalytic volume, and the HDS catalyst was dense loaded in the remaining three reactors (see Fig. 1 for the process flow-diagram).

Table 3
Experimental conditions of catalytic tests

Step	Sulfiding	Atmospheric residue	Boscan crude petroleum
Total pressure (Mpa)	15	15	15
Catalyst volume (cm^3)	40	40	40
Relative LHSV	1	0.5	1
H_2/oil (L/L)	400	1200	1200
Temperature (K)	623	643	663
Time-on-stream (h)	4	300	Variable

Table 4
Main process variables of interest for Cycle C

Total pressure (Mpa)	14
H_2/oil	
Recycle + make-up	Base
Quench to inlet R1B	Base × 0.63
Quench to inlet R2	Base × 0.48
Quench to inlet R3	Base × 0.63
Quench to inlet R4	Base × 0.55
Quench to inlet R5	Base × 0.30

The VR feedstock properties are listed in Table 2. The main objective of the refiner for that cycle was to produce a ULSFO with maximum 0.5 wt% sulfur. A very stable production meeting this objective was achieved after the first week of cycle C, the time necessary to achieve complete sulfidation of the sizeable catalytic mass, and hydrodynamic and thermal stabilisation of the complete unit (Fig. 6).

Table 4 summarizes the main process variables of interest maintained during this part of cycle C: total pressure, recycle + make-up and quench gas relative specific flow-rates: on this HYVAHL unit, quenches are located at each reactor outlet.

3. Results

3.1. Comparison of simulations results with bench scale aging tests results

3.1.1. Reproduction of fresh catalysts textural properties with random particle models representations

Tables 5 and 6 present the inputs to THERMIDOR, and results of the initial identification stage, for A and B catalysts, respectively.

For B, the computed and experimental average pore diameters (abscissa of the point of inflexion on the mercury

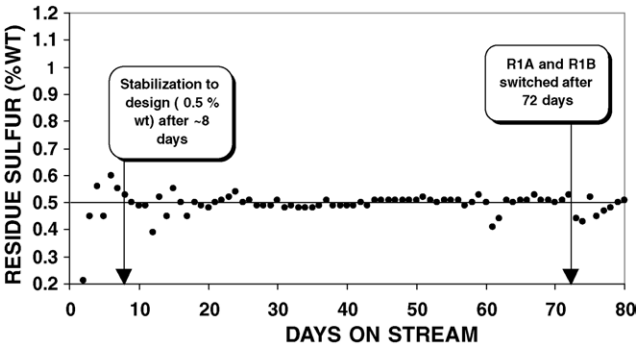

Fig. 6. Sulfur in residue at HYVAHL unit outlet during first part of cycle C.

Table 5
Results of identification of catalyst A geometrical properties to the RN2D "chesnut bur" model within THERMIDOR

Input	
Fresh catalyst total pore volume ($cm^3\ cm^{-3}$)	0.768
Fresh catalyst macropores volume ($cm^3\ cm^{-3}$)	0.238
Fresh catalyst mesopores volume ($cm^3\ cm^{-3}$)	0.530
Fresh catalyst total surface area ($cm^2\ cm^{-3}$)	0.952×10^6
Fresh catalyst mean macropores diameter (nm)	5000
Fresh catalyst mean mesopores diameter (nm)	25
Grain shape/mean grain radius (–/mm)	Spheres/0.885
Aspect ratio for 2D RN (*b*/*e*)	10
Output	
Effective bur density (cm^{-3})	0.117×10^{13}
Bur external radius (nm)	537.7
Number of platelets per bur	1368
Half-width *b* of platelets (nm)	32

porosimetry curve, Fig. 5) are 9 and 11 nm, respectively. For a set of six different monomodal HDS catalyst, with pore diameters ranging between 9 and 15 nm, we have obtained by a similar calibration with respect to the RCM, with $b/e = 5$, an average deviation of −12.5%. For this catalyst, with a deviation of −18.5% we are in the upper range. Nevertheless, the agreement is still quite satisfying.

For A, the average bur diameter obtained at around 1 μm is at least of the order of magnitude which can be estimated from the SEM micrograph on Fig. 5, whereas the dimensions of platelets are compatible with those observed by TEM and published elsewhere [11].

3.1.2. Fit of deactivation curves

Figs. 7–10 show the comparisons of simulated and experimental deactivation curves for HDM and HDS, and A and B, respectively. The following strategy was applied in order to achieve these fits:

1. The feedstock was crudely represented by four reactive components only in three chemical classes: 1 sulfur compound, 1 metal compound and 2 asphaltenic compounds: A1 and A2. The A1 component is a "small" asphaltene, responsible for coke deposition, and which does not inhibit the other reactions. It accounts for 90% of all asphaltenes. The A2 component is a "large" asphaltene, which strongly inhibits the other reactions, and accounts for 10% of the total asphaltene content specified. This particular choice relies on a principle of maximal simplicity and an ensemble of experimental observations: indeed, coke deposition does not seem to be limited by intragranular diffusional limitations, as testified by the absence of significant gradients in radial carbon profiles measured by microprobe analysis on a variety of used catalysts, whatever the pore size distribution. On the contrary, the systematic occurrence of maxima in V or Ni profiles inside the grains may be interpreted by the presence of a species which is a minoritary component but a strong inhibitor of HDM reactions, itself subject to strong diffusional limitations [13]. Besides, a fraction of asphaltenes does inhibit strongly all hydrotreating reactions, as shown for instance by the strong decrease of activities on hydrotreating deasphalted oils, when the amount of trace asphaltenes is increased in these feedstocks.

Table 6
Results of identification of catalyst B geometrical properties to the Random Coins Model within THERMIDOR

Input	
Fresh catalyst total pore volume ($cm^3\ cm^{-3}$)	0.639
Fresh catalyst total surface area ($cm^2\ cm^{-3}$)	2.852×10^6
Fresh catalyst mean mesopore diameter (nm)	11
Grain shape/mean grain radius (–/mm)	Cylinders/0.565
Aspect ratio for 3D RC (*b*/*e*)	5
Output	
Coin radius (nm)	15.8
Coin thickness (nm)	3.16
Coin density (cm^{-3})	0.918×10^{18}
Calculated mean mesopore diameter (nm)	9

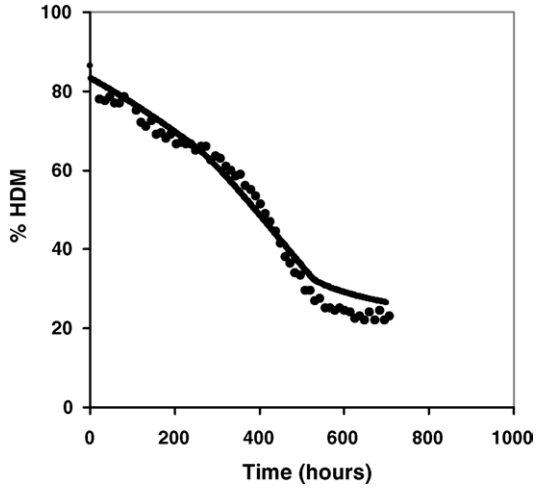

Fig. 7. Experimental (dots) vs. simulated (continuous) deactivation curves in HDM for bench scale isothermal hydroprocessing ageing tests on Boscan crude. Catalyst: A.

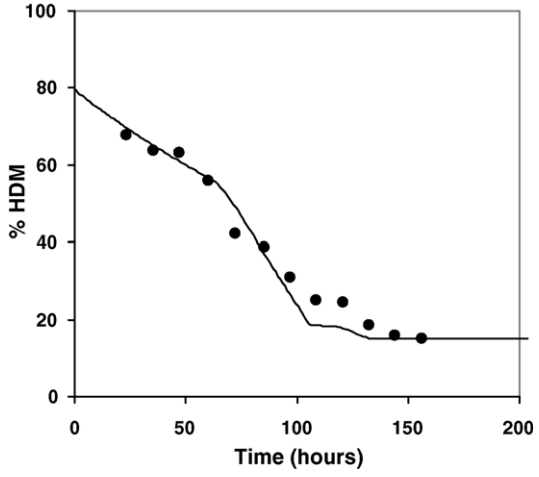

Fig. 8. Experimental (dots) vs. simulated (continuous) deactivation curves in HDM for bench scale isothermal hydroprocessing ageing tests on Boscan crude. Catalyst: B.

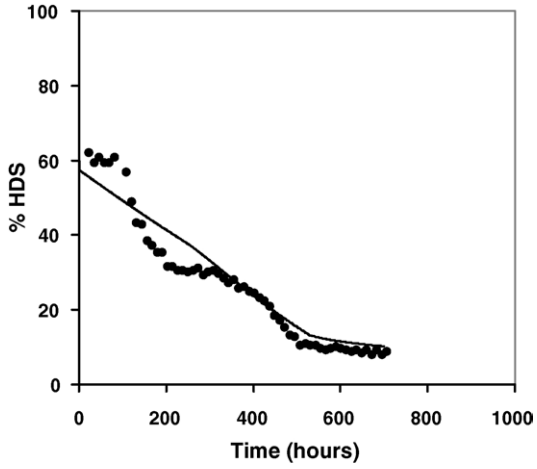

Fig. 9. Experimental (dots) vs. simulated (continuous) deactivation curves in HDS for bench scale isothermal hydroprocessing ageing tests on Boscan crude. Catalyst: A.

2. All parameters relative to the feedstock properties are fixed to the same values for both catalysts. A particularly strong constraint under this respect was to fix the parameter D_{ij}^{0m} to a common value D^{0m} for all species, so that differences in effective diffusivities originate through the function g either from the differences in molar masses, or in the catalysts initial textural properties and degree of fouling. The figure of 15×10^{-5} cm^2 s^{-1} retained for D^{0m} is quite consistent with the experimental value of 4.2×10^{-5} cm^2 s^{-1} reported for toluene in hexane at 25 °C [14].
3. Parameters relative to intrinsic catalysts properties (k_{ij}^0, K_{A2}^{0ads}) are adjusted, consistently with relative values obtained in separated tests involving mixtures of simple model molecules.
4. Lastly, the standard free energy ΔG_{coke}° of the coke forming equilibrated reaction was set so as to allow post-run predicted and experimental carbon contents to match, and considering that the intrinsic kinetic constants k_{coke}^0 are allowed to differ for the two catalysts.

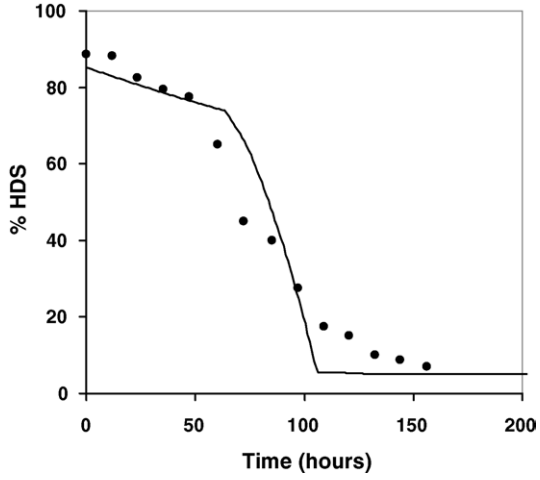

Fig. 10. Experimental (dots) vs. simulated (continuous) deactivation curves in HDS for bench scale isothermal hydroprocessing ageing tests on Boscan crude. Catalyst: B.

The set of parameters leading to the fits shown in Figs. 7–10 is given in Table 7. Notice that no attempts were made to find an optimum fit in the sense of a least square objective function. Notice also that the post-run experimental coke contents are rather moderate, and even surprisingly low for A (5.6 wt% C on the basis of the fresh catalysts after 700 h to be compared with 9.7 wt% for B after 150 h). This is in accordance with the known outstandingly low propensity of catalysts characterized by the "chesnut bur" texture, to promote coke formation in heavy ends hydroprocessing conditions.

3.2. Comparison of simulation results with data from the cycle C industrial run

3.2.1. Choice of parameters

The appropriate textural and geometrical parameters were calibrated in THERMIDOR for the industrial HDM and HDS catalysts.

As indicated by the comparison of properties in Table 2, BCP and industrial VR feedstocks are significantly different in nature, and therefore in reactivity. Of particular significance is the very high CCR content of the industrial VR, indicative of a very high propensity to generate coke in hydroprocessing conditions. These differences were accounted for in THERMIDOR by an adjustment of the fresh catalysts' initial intrinsic rate constants, so as to match as closely as possible the level of temperature at R1A inlet in stabilised industrial operation. In addition, the higher tendency to produce coke with VR was accounted for by increasing by a factor ~50 the equilibrium constant pre-factor in

Table 7
Parameters retained in THERMIDOR for the best fit of simulated and experimental HDM and HDS deactivation curves in bench scale ageing tests with Boscan crude as feedstock

Parameter	Metals	Asphaltene A1	Asphaltene A2	Sulfur
Feedstock description				
Fraction (%)	100	90	10	100
M (g mol^{-1})	2×10^3	10^3	1.2×10^5	10^3
D^{0m} (cm^2 s^{-1})	15×10^{-5}	15×10^{-5}	15×10^{-5}	15×10^{-5}
$E^{\pm diff}$ (cal mol^{-1})	3288	3288	3288	3288
T_0 (K)	400	400	400	400
ΔH (cal mol^{-1})	0	0	0	0
ΔH_{coke}° (cal mol^{-1})	0	5×10^3	0	0
$\exp(\Delta S_{coke}^{\circ}/R)$ (bar)	0	6×10^7	0	0
A catalyst description				
k^0 (cm s^{-1})	3.9×10^4	10^3	5×10^5	16.5×10^3
$E^{\pm}$ (cal mol^{-1})	4×10^4	4×10^4	4×10^4	4×10^4
K^{0ads} (cm^3 mol^{-1})	0	0	4.5×10^{12}	0
ΔH^{0ads} (cal mol^{-1})	0	0	1.5×10^4	0
k_{coke} (cm s^{-1})	0	2.2×10^3	0	0
$E_{coke}^{\pm}$ (cal mol^{-1})	0	4×10^4	0	0
B catalyst description				
k^0 (cm s^{-1})	5×10^4	10^3	10^6	5×10^3
$E^{\pm}$ (cal mol^{-1})	4×10^4	4×10^4	4×10^4	4×10^4
K^{0ads} (cm^3 mol^{-1})	0	0	5×10^{12}	0
ΔH^{0ads} (cal mol^{-1})	0	0	1.5×10^4	0
k_{coke} (cm s^{-1})	0	1.3×10^4	0	0
$E_{coke}^{\pm}$ (cal mol^{-1})	0	4×10^4	0	0

Table 8
Parameters retained in THERMIDOR for the simulation of cycle C industrial operations with VR as a feedstock

Parameter	Metals	Asphaltene A1	Asphaltene A2	Sulfur
Feedstock description				
Fraction (%)	100	90	10	100
M (g mol^{-1})	2×10^3	10^3	1.2×10^5	10^3
D^{0m} (cm^2 s^{-1})	15×10^{-5}	15×10^{-5}	15×10^{-5}	15×10^{-5}
$E^{\pm diff}$ (cal mol^{-1})	3288	3288	3288	3288
T_0 (K)	400	400	400	400
ΔH (cal mol^{-1})	0	10^5	10^5	10^5
ΔH°_{coke} (cal mol^{-1})	0	5×10^3	0	0
$\exp(\Delta S^{\circ}_{coke}/R)$ (bar)	0	2.75×10^9	0	0
Industrial HDM catalyst description				
k^0 (cm s^{-1})	5×10^4	10^4	5×10^5	2×10^3
$E^{\pm}$ (cal mol^{-1})	4×10^4	4×10^4	4×10^4	4×10^4
K^{0ads} (cm^3 mol^{-1})	0	0	4.5×10^{12}	0
ΔH^{0ads} (cal mol^{-1})	0	0	1.5×10^4	0
k_{coke} (cm s^{-1})	0	2.2×10^3	0	0
$E^{\pm}_{coke}$ (cal mol^{-1})	0	4×10^4	0	0
Industrial HDS catalyst description				
k^0 (cm s^{-1})	3.9×10^4	1.5×10^4	10^6	3×10^3
$E^{\pm}$ (cal mol^{-1})	4×10^4	4×10^4	4×10^4	4×10^4
K^{0ads} (cm^3 mol^{-1})	0	0	5×10^{12}	0
ΔH^{0ads} (cal mol^{-1})	0	0	1.5×10^4	0
k_{coke} (cm s^{-1})	0	10^3	0	0
$E^{\pm}_{coke}$ (cal mol^{-1})	0	4×10^4	0	0

Eq. (6) for asphaltene A1 in order for simulated coke level to match that measured at inlet of R1A at EOR. Table 8 presents the set of parameters input to THERMIDOR for simulating cycle C according to these criteria.

3.2.2. Temperature profiles

In Fig. 11a are shown the evolution with time on stream of temperatures recorded at selected points in the industrial unit: inlets of reactors R1A, R2, R3 and outlet of R5. The simulated counterparts are presented in Fig. 11b. Inlet of R3 is the coolest point of the HYVAHL unit both in reality and in simulation while inlet and outlet temperatures are maintained at comparable levels by the use of quenches.

Fig. 12a shows longitudinal temperature profiles as recorded at times 8 days (stabilisation of the unit, or SOR), 45 days (approximate middle of run or MOR) and 72 days (end of run before guard bed switch or EOR). The corresponding simulated profiles are shown in Fig. 12b. The magnitudes of exothermicities, as recorded from outlet minus inlet temperatures in the different reactors in series, and the temperature drops caused by quench boxes as recorded by outlet of reactor q minus inlet of reactor $q + 1$ can be compared to simulated levels from these two figures. The sum of exothermicities recorded on the unit is close to 75 °C on average for stabilised operations, while 60 °C is achieved in simulation. Simulated temperature drops upon quenching amount also to 80–85% of recorded values. We did not try to achieve much better correspondence in view of the relative crudeness of our representation of the feedstock and rate equations. In particular, recorded exothermicities in the

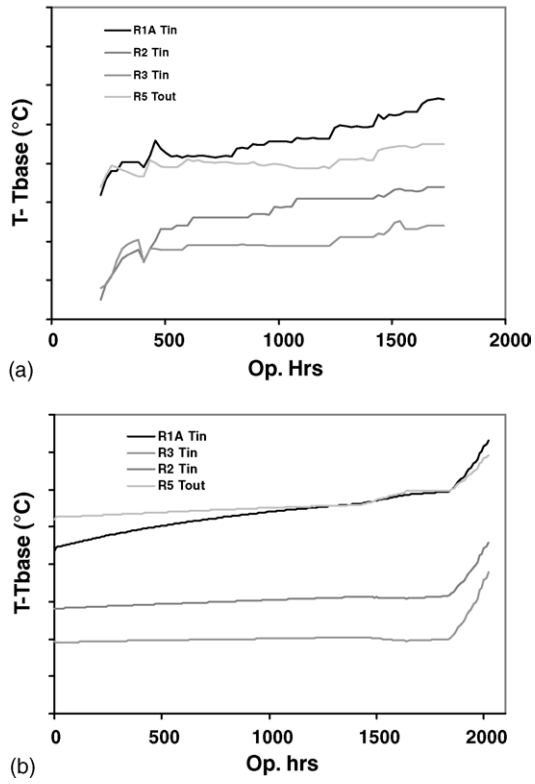

Fig. 11. Evolution with time on stream of temperatures at inlets of R1A, R2, R3 and outlet of R5: (a) as recorded on the industrial unit; (b) from simulation. (Temperature intervals in ordinates: 10 °C.)

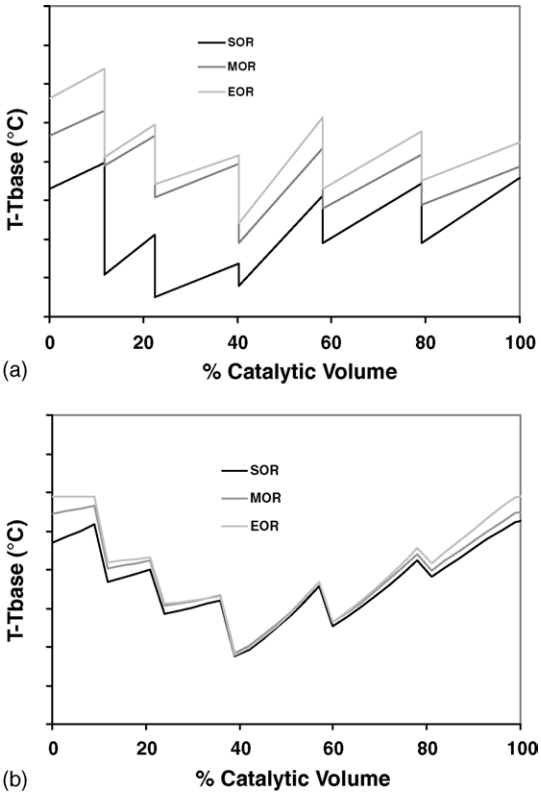

Fig. 12. Longitudinal temperature profiles at times 8 days (stabilisation of the unit, or SOR), 45 days (approximate middle of run or MOR), and 72 days (end of run before guard bed switch or EOR). (a) As recorded on the industrial unit and (b) from simulations. (Temperature intervals in ordinates: 10 °C.)

HDM reactors tend to be systematically superior to those predicted by simulations.

3.2.3. Simulated longitudinal profiles in coke, metal sulfides, Tamm factor, surface area and porosity as a function of time

Fig. 13a–e show these simulated longitudinal profiles at SOR, MOR and EOR (see above). Coke contents measured on samples taken from R1A at EOR are also reported in Fig. 13a. The factor of Tamm [15] is the ratio of average to maximal radial concentration of deposited metals (e.g. V) in a catalyst grain. Therefore, this factor is close to one for a gradientless deposition, and tends towards zero as the efficiency of intragranular mass transfer decreases, favoring pore mouth plugging. These figures show clearly the differences between the 2 + 1 lead beds loaded with the HDM catalyst and the last three beds, loaded with the HDS catalyst: the former efficiently capture by far the largest fraction of metals, with high Tamm factors, while the latter are hardly affected, but remain characterized by very low Tamm factors. In addition, the persistence of total pore volume and surface areas close to the fresh catalysts values for the three last beds is indicative of the effective protection ensured by the lead HDM catalyst.

3.2.4. Simulated radial profiles at different locations and times

Fig. 14a–f show simulated normalised radial concentrations profiles at R1A inlet and R5 outlet for SOR, MOR and EOR. These graphs allow us to characterize the different regimes of mass transfer coupled to chemical consumption assigned to the

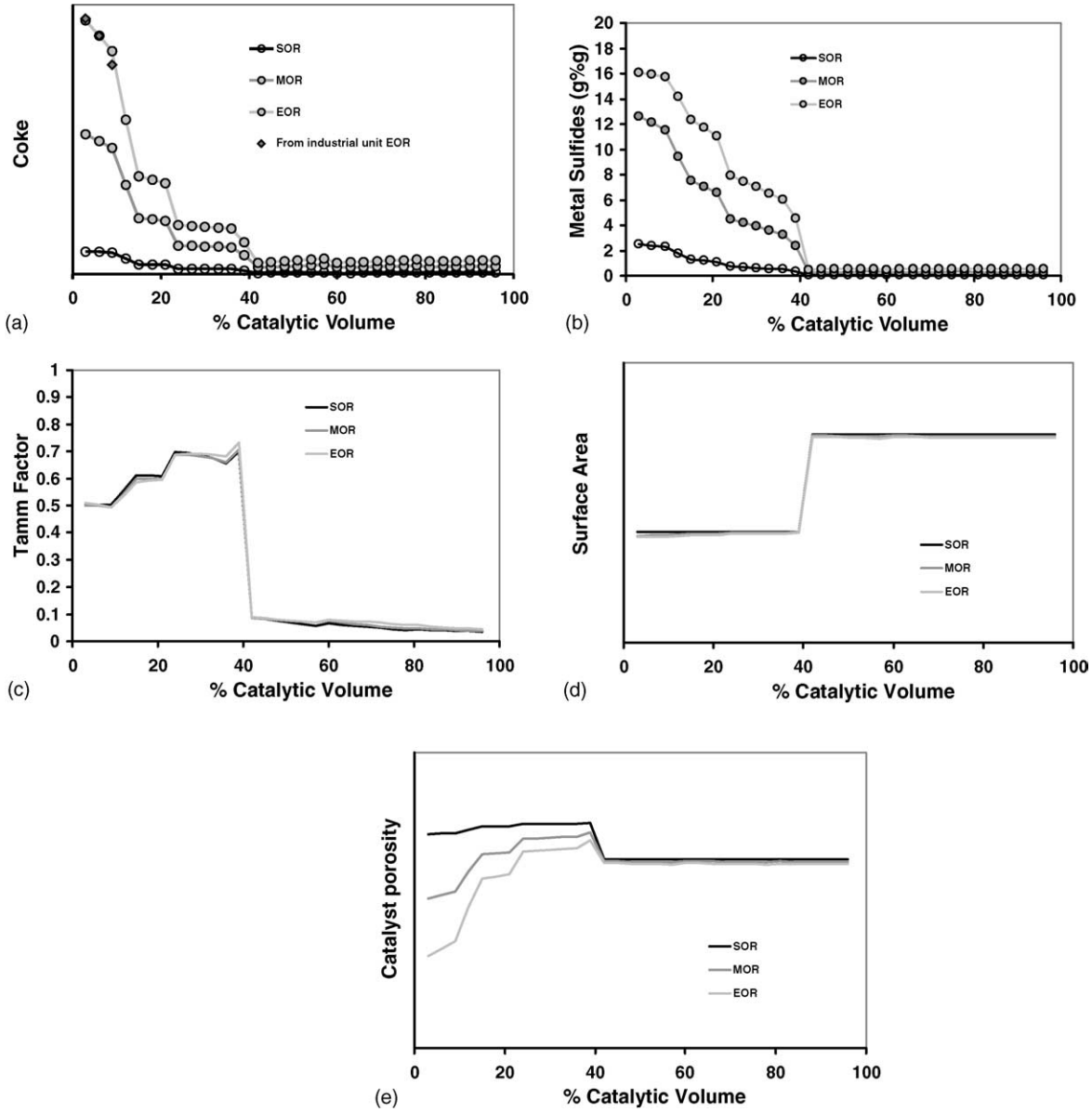

Fig. 13. Simulated longitudinal profiles in (a) coke (filled rhombs, analysis of unloaded catalyst from the industrial unit), (b) metal sulfides, (c) Tamm factor, (d) surface area and (e) porosity as a function of time for industrial cycle C.

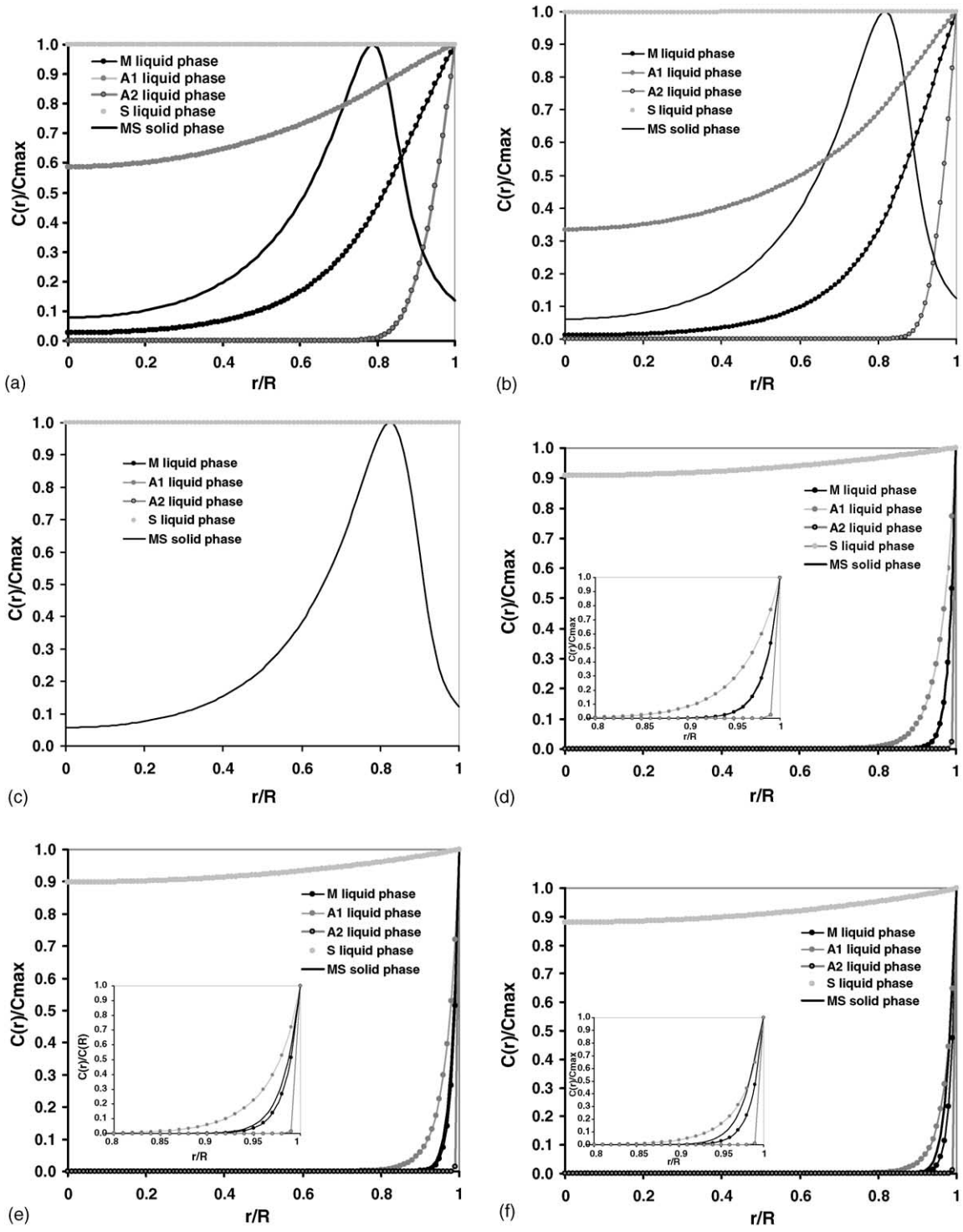

Fig. 14. Simulated normalized radial concentrations profiles at R1A first layer (a) SOR, (b) MOR, (c) EOR and R5 last layer (d) SOR, (e) MOR and (f) EOR. C(R) is the concentration within the outermost layer of catalyst grain. (Insets in (d–f)) presents zooms on the region r/R [0.8–1.0]).

interplaying pseudo-reactants, the S bearing, M bearing and A1 and A2 asphaltenic compounds, depending on the catalyst (lead HDM, tail HDS) and its age. Weak or absent internal mass transfer limitations always characterize the HDS and HDA1 reactions for both catalysts, while very strong concentration gradients in A2 determine peripheral inhibition of all reactions: the inward extent of the inhibition zone is more pronounced for the lead HDM catalyst, which possess macropores, allowing deeper penetration of the large A2 asphaltenes. As a consequence the metal deposition profiles, which trace the time integrated local rate of HDM, present a maximum at a lower fractional radius for the HDM catalyst. In the latter, the concentration gradient is, however, much weaker for M in liquid phase than in the HDS catalyst.

3.3. Simulation of the influence of the partition between HDM and HDS catalysts on the run duration before the first permutation of guard reactors

Fig. 15 shows the simulated run lengths as a function of the volumetric fraction of HDM catalyst loaded in the six successive reactors. The proportion fixed by design on the basis of extensive pilot plant experimentation for a typical industrial unit is the lead 40%, that is as seen above R1A + R1B + R2, loaded with the HDM catalyst. For the simulations, we have maintained all inputs constant, including quench gas specific flow-rates at reactor outlets. Therefore, in Fig. 15, 0% corresponds to HDS catalyst dense loaded everywhere, and 100% to no HDS catalyst at all. Simulations were run for a discrete set of volume fractions (full dots). The dotted line is a mere guide for the eye. The run length is defined according to the maximum temperature criterion, that is a simulation stops whenever temperature reaches the maximum allowed somewhere in the unit. Open symbols mark the time needed to reach another criterion, a prescribed maximum amount of coke $C^{s}_{coke,max}$ in the first layers of the lead reactor, in the case it happens first. This amount is that reached in reality at EOR (just before switching R1B and R1A), that is when pressure drop reached an upper limit sustainable by the main recycle compressor.

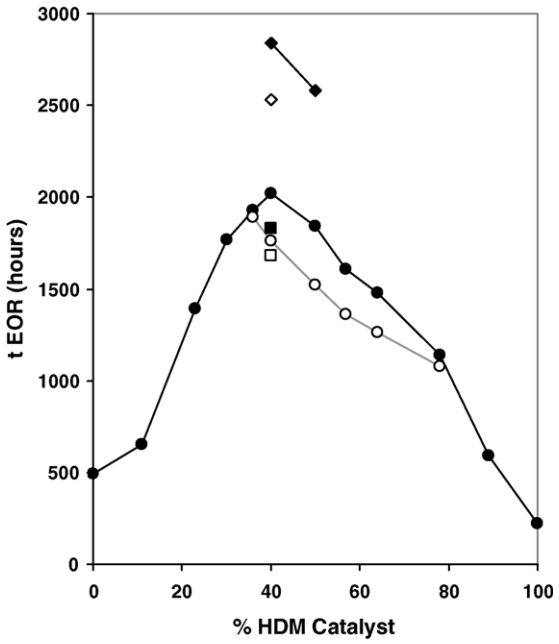

Fig. 15. Simulated initial cycle length before permutation of R1A and R1B, in typical HYVAHL conditions (cycle C) for Vacuum Residue desulfurization, as a function of the fraction of HDM catalyst in the HDM + HDS combination. Full circles, 0.5 wt% in the liquid fuel produced with EOR at hottest spot at T_{max} (EOR1). A distinct maximum in cycle length appears at 40 vol% of front HDM catalyst, the typical proportion adopted at the industrial scale. Open circles, same, but time for EOR at $C^{s}_{coke,max}$ at top of guard bed (EOR2). Full/Open square: cycle length at optimum combination for 0.3% S in liquid product EOR1/EOR2. Full/Open rhombs, cycle length for 0.3% S in liquid product with the combination of new catalysts EOR1/EOR2. A increase of initial cycle length by more than 50% is predicted. (The interpolation lines are mere guides for the eye.)

4. Discussion of results

The results presented above show to what extent numerical simulations based on the present stage of development of THERMIDOR can account for residue hydroprocessing in fixed beds. Our model is both sophisticated, with respect to the description of catalysts and their deactivation, and still crude, with respect to the description of reaction pathways and their kinetics. For that reason, we have not gone beyond a semi-quantitative match of industrial temperature records, but rather tried to reproduce consistently the most salient features of the unit's behaviour, including the evolution of catalysts according to their nature, position and time.

Figs. 7 and 8 allow us to compare the deactivation characteristics of the HDM (A) and HDS (B) catalysts, respectively with respect to the HDM reaction. Notice first the difference in time scales, which shows that in these bench scale ageing test conditions, the HDM catalyst resists about five times longer than the HDS catalyst to exposure to metals. The same is true for the HDS reaction as shown in Figs. 9 and 10, but as expected, the HDS catalyst is much more selective than the HDM catalyst for that difficult reaction, as long as its pore mouths are not plugged. The relatively rapid deactivation induced by the pore mouth plugging phenomenon extends over about 50 h, the time necessary for the ''wave'' of poisoning to sweep across the entire bed, which does not work here in gradientless conditions, except for temperature.

The comparison of temperatures recorded at different locations during industrial operations, and provided by simulation (Fig. 11a and b), shows a better agreement beyond 500 h, while apparently a faster initial deactivation had to be compensated for in real operation. The inlet temperature is then increased at similar rates in reality (∼13 °C/1000 h) and simulation (∼9 °C/1000 h). The minimum temperature in the unit is soon located at inlet of R3 (inlet of HDS section), both in reality and simulation, at the very stable level of about T_{base} + 20 °C: this stability reflects the efficiency of the HDM section in providing a stable input to the HDS section.

As mentioned above, in actual operations the record terminates after 72 days (1730 h) when pressure drop across R1A has reached a critical threshold: R1B and R1A are then permuted thanks to the PRS design, and the cycle goes on, while R1A is rejuvenated before being inserted again in second position. The simulation was pursued in the initial configuration until the maximum temperature T_{max} was reached at outlet of R1A: a phase of final deactivation appears in Fig. 11b beyond circa 1850 h characterized by a faster rise of inlet temperature, and as a consequence of all temperatures, since quench flow-rates are kept constant.

The longitudinal temperature profiles at SOR, MOR and EOR are shown in Fig. 12a for actual operations and Fig. 12b for simulations: the discrepancies reflect, as already mentioned, an underestimation in simulations of both the exothermicities of reactions and the effect of quenches. Records archived from industrial units comprise inlets and outlets of each reactor only, so that profiles within a reactor are approximated by straight segments. Simulated profiles are more resolved, and show a positive curvatures upwards, which is confirmed by actual records

whenever temperature probes are available at different levels in a reactor. In order to improve the estimation of exothermicites, it should be necessary to adopt a more accurate description of both the inventory of reactions and their kinetics, as we plan to implement in future releases of THERMIDOR. In particular, hydrocracking reactions take place mostly along the first reactors in the HDM section, and contribute significantly to an exothermicity, but these reactions were not accounted for in the simulations.

The noticeable discrepancy seen on comparing again Fig. 11a and b, between recorded and simulated SOR temperatures might stem in part from underestimated initial exothermicities, in particular as regards hydrocracking reactions, which possibly undergo a specific and much faster deactivation rate. Obviously THERMIDOR in its present state of development does not account for this very initial stage of deactivation which deserves further analysis. Notice that this phenomenon does not really show up in pilot plant experiments. It remains to be precisely determined whether the corresponding steep rise of temperatures between 250 and 300 h of operation really reflects a deactivation of the catalysts or rather the last stage of hydrodynamic and thermal equilibration of the whole unit. It is also possible to invoke delays in the monitoring loop (e.g. induced by sampling lines, furnace inertia, etc.) so that dynamic simulation explicitly taking such delays into account should be necessary in order to reproduce correctly the phenomenon.

In addition, the simulated exothermicity in R5 is about twice (in terms of ΔT) the actual one, which should be attributed mostly to the removal of the less reactive sulfur compounds achieved in this section. Since our simulation assumes a simple order 1 kinetics with respect to sulfur, it overestimates the % HDS achieved by R5 and therefore the associated heat release. Again, a more detailed kinetic model should be able to cure this defect.

The simulation of quench efficiencies should be more accurate with precise data on quench gas composition and temperature, unfortunately not available from the plant.

Simulated longitudinal profiles of deposited coke are shown in Fig. 13a for SOR, MOR and EOR: these profiles emphasize the relatively rapid build-up of coke in the HDM section, and particularly across R1A, the guard reactor. By contrast, the HDS section is hardly affected by coke deposition during this initial part of cycle C. Interestingly, the simulated profile at EOR matches very well the actual one, as determined from elemental analysis of used industrial HDM catalyst sampled at inlet, mid-reactor and outlet of R1A after permutation with R1B.

The other profiles have been already commented in Section 3.2.3: we can add that the increase in the factor of Tamm with increasing depth in the HDM section is a consequence of decreasing temperatures (Fig. 12b) and decreasing local concentration in metals, so that radial gradients in metal deposition at the catalyst grain level decrease. Tamm factors appear remarkably stable with time on stream. Specific areas are also stable, while porosities in the HDM section decrease, as expected, with increasing coke and metal sulfide deposition, so that the larger loss is simulated for R1A at EOR. The residual porosity in R1A at EOR approaches a limiting lower value, which means that at this stage only macroporosity is left. Interestingly, surface areas in the HDM section appear almost unaffected by coke and metal sulfides deposits: indeed, according to the description adopted in THERMIDOR, the loss of surface area due to coverage of fresh catalyst by particles of coke and metal sufides is initially compensated by the increase of surface area brought about by the growth of these particles.

The simulated radial concentration profiles shown in Fig. 14a–f are particularly significant. In the first layer of HDM catalyst in R1A, we notice that the concentration in S remains gradientless from SOR to EOR, that is to say HDS is limited by kinetics and not by intragranular mass transfer. Actually a concentration step occurs for sulfur between liquid phase outside the grain boundary, and liquid phase in the first layer of grains, not shown in the figures. The same is not true for the last layer of HDS catalyst in R5, where the combination of high temperature and high activity induces the onset of some diffusional limitations to HDS from SOR to EOR (Fig. 14d–f). For metals, our choice of parameters for the simulations leads to diffusional limitations in all cases, although much more marked for the HDS catalyst. Asphaltenes of type 1 are relatively unreactive and have a small radius of gyration, so that their elimination is less limited by mass transfer than that of metals. Moderate to weak radial gradients of coke deposition will show up as a direct consequence. Asphaltenes of type 2 are set with large radii of gyration so that their elimination is severely limited by mass transfer. Moreover, these compounds are assumed to inhibit strongly all other reactions, so that following their steep radial concentration gradient a steep gradient of inhibition appears from the external grain boundary towards the center, in the first outer layers. This phenomenon is neatly recorded by the radial distribution of metals sulfides in the HDM catalyst (Fig. 14a–c), which presents a steep maximum between fractional radii $r/R = 0.8$ and 0.85. The shape of this distribution does not vary significantly between SOR and EOR, however, the maximum amount of metal sulfides deposited does increase from 2 g%g to 16 g%g (Fig. 13b). The latter amount is again in good agreement with the elemental analysis obtained for the sample of R1A top layer after EOR. As previously reported [13], such distribution of metals deposited in used HDM catalysts, peaked at some fractional radius below one, is quite commonly observed upon microprobe analysis of polished cross-sections.

Finally, Fig. 14c shows the disappearance of concentration gradients for all reactive species (S, A1, A2 and M), or in other terms $C(r)/C(R^G) = 1$ for $r/R^G \leq 1$: this reflects the complete or nearly complete loss of activity in mesopores of this severely deactivated catalyst, while the still free and open macropores allow reactants to reach the grain center.

Fig. 15 shows that whatever the EOR criterion, the maximum cycle length is obtained for a volume fraction close to the typical industrial design of 40%. This maximum is quite well defined, which means that cycle length drops significantly either when the HDS catalyst is not protected enough by a sufficient amount of HDM catalyst, or when the amount of HDS catalyst is too low to allow the specification of maximum sulfur in effluent to be sustained. Deviations from the optimal volume fraction strongly affect the cycle length.

Fig. 15 also shows the somewhat lower simulated cycle length achieved at HDM catalyst volume fraction 40% when the more severe target of 0.3 wt% S in the fuel produced is assigned. Finally, this cycle length for producing ULSFO at 0.3% S is predicted to increase by 54% when a new generation of catalysts is involved. These new catalysts exhibit intrinsic activities approximately 1.5 times higher than their earlier counterparts. The simulations reflect therefore the effect of increasing all specific activities of the fresh catalysts by this amount, keeping all other input parameters constant.

5. Conclusions

We have presented THERMIDOR, a new model aiming at predicting the cycle length of fixed-bed residue hydroprocessing units, and have compared results of numerical simulations based on this model with representative data of industrial operations at full scale of the HYVAHL process.

This process combines different specific catalysts in order to maximize both performance and cycle length, although these catalysts are exposed to different causes of severe deactivation: inhibition and poisoning of active phases, pore plugging by products of trace organometallic decomposition, and by coke formed from dehydrogenation and polycondensation side reactions. Stable operations according to the specific objectives of the refinery can nevertheless be achieved thanks to, on the one hand, the careful chemical and physical design of catalysts including pore shapes and pore size distributions, and on the other hand the process design. For the latter, salient features are the introduction of the permutable guard reactors system (PRS), the adequate dimensioning of the multiple high pressure reactors placed in series, with intermediate heat transfer (quenches), and the crucial definition of the proportion and location of the different catalysts in the reactors.

Since in HYVAHL catalysts and process design aiming at maximal cycle length are intimately coupled problems, THERMIDOR simulations address these problems simultaneously, taking into account all relevant spatial and temporal scales.

Simulations are validated at three levels:

1. Representations of the fresh catalysts by random object models are fitted to available textural data.
2. The chemical model involving the representation of residues feedstocks by lumped reactive species, the associated physicochemical and kinetic properties, and a choice of parameters representing the kinetic and geometrical aspects of deactivation phenomena, is adjusted by comparison to the experimental results of ageing tests under Boscan crude in isothermal conditions.
3. In the last step, the adjustment of textural and kinetic parameters accounting for the specific catalysts and feedstock used in industrial operations is necessary in order to reproduce the full scale unit behaviour in terms of cycle lengths, temperature and catalyst properties profiles as a function of position and time.

These three steps have been illustrated, and the predictive power of THERMIDOR is finally demonstrated with the localisation of the typical optimum partition between HDM and HDS catalysts, in excellent agreement with that deduced from extensive experimental studies.

For an ever more realistic simulation of such a complex process as fixed-bed residue hydroprocessing, THERMIDOR gives very encouraging results, yet many improvements are still ahead. As discussed above, the interplay of catalytic and non catalytic phenomena causing pressure drop drift across the lead guard bed should be better understood so that a mathematical model can be developed and implemented in the simulator. Besides, although the present version allows for a rather sophisticated description of the feedstock in terms of lumped reactive species and the associated kinetic parameters, we have not yet fully explored its potential and limits. For instance, it is well known that heteroatom removal from hydrocarbon feedstocks by hydrotreating can be described by simple kinetics of fractional apparent order comprised between one and two with respect to the concentration in heteroatoms: it is possible to rationalise this observation under the assumption that for a group of reactive species, e.g. sulfur compounds, kinetics of order one are obeyed for each compound, while the reactivities follow some peaked distribution, e.g. Gamma or log-normal [16]. Therefore, it is already in principle possible in THERMIDOR to fine-tune the model distribution of species and associated reactivities so as to reproduce experimental apparent orders, or in other terms to better predict the important correlations of performance versus contact time. However, phenomena of mutual inhibition are also very important in hydrotreating, such as described in the present report for the effect of ‘‘large’’ asphaltenes (A2) on the kinetics of other reactions. We plan therefore to adopt Langmuir–Hinshelwood kinetics for all reactions in THERMIDOR, according to a lumping strategy and simplified reaction scheme already established through a significant experimental work [17]. Finally, it is our opinion that Eqs. (12)–(14) do not provide the most satisfactory description of effective diffusivity in porous media. We are currently developing an alternative approach, based on Monte Carlo simulations of random walks in random porous media.

Acknowledgments

We are indebted to Cécile Plain and Olivier Le Coz from AXENS for providing operational data. Sébastien Gachadouat from Direction des Etudes Economiques, IFP, is acknowledged for his studies of the fuel market. We thank Prof. John Lynch, IFP, for his advices and careful reading of the manuscript.

References

[1] (a) A. Billon, J.P. Peries, M. Espeillac, T. des Courrieres, NPRA 89th Annual Meeting, San Antonio, March 17–19, 1991;
(b) S. Kressmann, F. Morel, V. Harlé, S. Kasztelan, Catal. Today 43 (1998) 203.
[2] H. Toulhoat, R. Szymanski, J.C. Plumail, Catal. Today 7 (1990) 531.
[3] B. Smith, J. Wei, J. Catal. 132 (1991) 21.

[4] G. Gualda, S. Kasztelan, J. Catal. 161 (1996) 319.
[5] M.A. Anisimov, I.K. Yudin, V. Nikitin, G. Nikolaenko, A. Chernoutsan, H. Toulhoat, D. Frot, Y. Briolant, J. Phys. Chem. 99 (23) (1995) 9576.
[6] C.N. Satterfield, Mass Transfer in Heterogeneous Catalysis, MIT Press, Cambridge, 1970.
[7] J.C. Spry, W.H. Sawyer, 68th AIChE Annual Meeting, Paper 30C (1975).
[8] H.J. Weissberg, J. Appl. Phys. 34 (9) (1963) 2636.
[9] H.A.M. van Eekelen, J. Catal. 29 (1973) 75.
[10] O. Macé, J. Wei, Ind. Eng. Chem. Res. 30 (1991) 909.
[11] H. Toulhoat, Y. Jacquin, T. Dupin, US Patent 4,499,203. (1985).
[12] J.H. Perry, Chemical Engineer's Handbook, fourth ed., Mc Graw-Hill, New York, 1963, 3-133.
[13] I. Tanoubi, P. Martinerie, P. Bourseau, G. Muratet, H. Toulhoat, Rev. Inst. Fra. Petr. 46 (3) (1991) 389.
[14] D.R. Lide, Handbook of Chemistry and Physics, 76th ed., CRC Press, Boca Raton, 1996.
[15] P.W. Tamm, H.F. Harnsberger, A.G. Bridge, Ind. Eng. Chem. Process Dev. 20 (1981) 262.
[16] R.H. van Dongen, D. Bode, H. van der Eijk, J. van Klinken, Ind. Eng. Chem. Process Dev. 19 (1980) 630.
[17] F.X. Haule, Ph.D. Thesis, University of Paris 6, 2002.